Unveiling the Cosmic Gems Arc at $z \sim 10.2$ with JWST

Larry D. Bradley,[1] Angela Adamo,[2] Eros Vanzella,[3] Keren Sharon,[4] Gabriel Brammer,[5,6] Dan Coe,[1,7,8]
Jose M. Diego,[9] Vasily Kokorev,[10] Guillaume Mahler,[11,12,13] Masamune Oguri,[14,15] Abdurro'uf,[8,1]
Rachana Bhatawdekar,[16] Lise Christensen,[5,6] Seiji Fujimoto,[17,*] Takuya Hashimoto,[18,19] Tiger Y.-Y Hsiao,[8]
Akio K. Inoue,[20,21] Yolanda Jiménez-Teja,[22,23] Matteo Messa,[3] Colin Norman,[24,1] Massimo Ricotti,[25]
Yoichi Tamura,[26] Rogier A. Windhorst,[27] Xinfeng Xu,[28,29] and Adi Zitrin[30]

[1]Space Telescope Science Institute (STScI), 3700 San Martin Drive, Baltimore, MD 21218, USA
[2]The Oskar Klein Centre, Department of Astronomy, Stockholm University, AlbaNova, SE-106 91 Stockholm, Sweden
[3]INAF–OAS, Osservatorio di Astrofisica e Scienza dello Spazio di Bologna, via Gobetti 93/3, I-40129 Bologna, Italy
[4]Department of Astronomy, University of Michigan, 1085 S. University Ave, Ann Arbor, MI 48109, USA
[5]Cosmic Dawn Center (DAWN), Copenhagen, Denmark
[6]Niels Bohr Institute, University of Copenhagen, Jagtvej 128, DK-2200 N, Copenhagen, Denmark
[7]Association of Universities for Research in Astronomy (AURA) for the European Space Agency (ESA), STScI, Baltimore, MD, USA
[8]Center for Astrophysical Sciences, Department of Physics and Astronomy, The Johns Hopkins University, 3400 N Charles St.
Baltimore, MD 21218, USA
[9]Instituto de Física de Cantabria (CSIC-UC). Avda. Los Castros s/n. 39005 Santander, Spain
[10]Kapteyn Astronomical Institute, University of Groningen, P.O. Box 800, 9700AV Groningen, The Netherlands
[11]Institute for Computational Cosmology, Durham University, South Road, Durham DH1 3LE, UK
[12]Centre for Extragalactic Astronomy, Durham University, South Road, Durham DH1 3LE, UK
[13]STAR Institute, Quartier Agora - Allée du six Août, 19c B-4000 Liège, Belgium
[14]Center for Frontier Science, Chiba University, 1-33 Yayoi-cho, Inage-ku, Chiba 263-8522, Japan
[15]Department of Physics, Graduate School of Science, Chiba University, 1-33 Yayoi-Cho, Inage-Ku, Chiba 263-8522, Japan
[16]European Space Agency (ESA), European Space Astronomy Centre (ESAC), Camino Bajo del Castillo s/n, 28692 Villanueva de la
Cañada, Madrid, Spain
[17]Department of Astronomy, The University of Texas at Austin, Austin, TX 78712, USA
[18]Graduate School of Pure and Applied Sciences, University of Tsukuba, 1-1-1 Tennodai, Tsukuba, Ibaraki 305-8571, Japan
[19]Tomonaga Center for the History of the Universe, University of Tsukuba, 1-1-1 Tennodai, Tsukuba, Ibaraki 305-8571, Japan
[20]Department of Physics, School of Advanced Science and Engineering, Faculty of Science and Engineering, Waseda University, 3-4-1
Okubo, Shinjuku, Tokyo 169-8555, Japan
[21]Waseda Research Institute for Science and Engineering, Faculty of Science and Engineering, Waseda University, 3-4-1 Okubo,
Shinjuku, Tokyo 169-8555, Japan
[22]Instituto de Astrofísica de Andalucía–CSIC, Glorieta de la Astronomía s/n, E–18008 Granada, Spain
[23]Observatório Nacional, Rua General José Cristino, 77 - Bairro Imperial de São Cristóvão, Rio de Janeiro, 20921-400, Brazil
[24]Department of Physics and Astronomy, The Johns Hopkins University, 3400 N Charles St. Baltimore, MD 21218, USA
[25]Department of Astronomy, University of Maryland, College Park, 20742, USA
[26]Department of Physics, Graduate School of Science, Nagoya University Furo, Chikusa, Nagoya, Aichi 464-8602, Japan
[27]School of Earth and Space Exploration, Arizona State University, Tempe, AZ 85287-1404, USA
[28]Department of Physics and Astronomy, Northwestern University, 2145 Sheridan Road, Evanston, IL, 60208, USA
[29]Center for Interdisciplinary Exploration and Research in Astrophysics (CIERA), Northwestern University, 1800 Sherman Avenue,
Evanston, IL, 60201, USA
[30]Department of Physics, Ben-Gurion University of the Negev, P.O. Box 653, Be'er-Sheva 84105, Israel

Submitted to ApJ

ABSTRACT

We present recent JWST NIRCam imaging observations of SPT0615-JD (also known as the Cosmic Gems Arc), lensed by the galaxy cluster SPT-CL J0615−5746. The 5″-long arc is the most highly

Corresponding author: Larry D. Bradley
lbradley@stsci.edu

magnified $z > 10$ galaxy known, straddling the lensing critical curve and revealing five star clusters with radii ~ 1 pc or less. We measure the full arc to have F200W 24.5 AB mag, consisting of two mirror images, each 25.3 AB mag with a magnification $\mu \sim 60$ (delensed 29.7 AB mag, $M_{UV} = -17.8$). The galaxy has an extremely strong Lyman break F115W$-$F200W > 3.2 mag (2σ lower limit), is undetected in all bluer filters ($< 2\sigma$), and has a very blue continuum slope redward of the break ($\beta = -2.7 \pm 0.1$), resulting in a photometric redshift $z_{\rm phot} = 10.2 \pm 0.2$ (95% confidence) with no significant likelihood below $z < 9.8$. Based on SED fitting to the total photometry, we estimate an intrinsic stellar mass of $M_* \sim 2.4 - 5.6 \times 10^7 M_\odot$, young mass-weighted age of $\sim 21 - 79$ Myr, low dust content ($A_V < 0.15$), and a low metallicity of $\lesssim 1\%$ $Z_\odot$. We identify a fainter third counterimage candidate within $2\farcs2$ of the predicted position, lensed to AB mag 28.4 and magnified by $\mu \sim 2$, suggesting the fold arc may only show $\sim 60\%$ of the galaxy. SPT0615-JD is a unique laboratory to study star clusters observed within a galaxy just 460 Myr after the Big Bang.

1. INTRODUCTION

The James Webb Space Telescope (JWST) was designed to peer into the distant Universe and study galaxies near the beginning of time. Early in its mission, JWST observations have already prompted us to reevaluate our understanding of the first phases of galaxy build-up, eventually leading to the reionization of the Universe. At early cosmic times and throughout the reionization era, galaxies appear to experience rapid starburst phases (Endsley et al. 2023; Boyett et al. 2024) and metal enrichment (Curti et al. 2023), merger events (Hsiao et al. 2023a; Asada et al. 2023), and harbor massive stars producing extreme ionization (e.g., Matthee et al. 2023; Atek et al. 2023). At redshift $z > 10$ ($t_{\rm Universe} < 470$ Myr), early galaxies appear to be more luminous than expected, suggesting conditions for which we have not accounted. Several explanations have so far been explored, including significantly higher star formation efficiency during their early assembly stages, a top-heavy initial mass function (IMF), and stochastic burst events (e.g, Adams et al. 2023a; Harikane et al. 2023; McLeod et al. 2023; Finkelstein et al. 2023a, among many others).

While JWST has already discovered many galaxies at $z > 9$ (e.g., Castellano et al. 2022; Naidu et al. 2022; Finkelstein et al. 2022; Adams et al. 2023a; Harikane et al. 2023; Bradley et al. 2023; Donnan et al. 2023; Atek et al. 2023; Finkelstein et al. 2023a; Robertson et al. 2023; Castellano et al. 2024; Hainline et al. 2024), most are too faint and small to be studied in detail. Most of these early galaxies will remain unresolved, with their stellar populations only inferred and never observed di-

rectly. Highly-lensed and spatially-resolved early galaxies (e.g., Bradley et al. 2023; Hsiao et al. 2023a; Roberts-Borsani et al. 2023; Stiavelli et al. 2023; Vanzella et al. 2023; Bradač et al. 2024) will provide the only chance to directly study the engines that reionized the Universe.

The combined powers of JWST and gravitational lensing have revealed small star clusters in a precious few highly-magnified distant galaxies at $4 < z < 8$ (e.g., Mowla et al. 2022; Claeyssens et al. 2023; Vanzella et al. 2022, 2023; Mowla et al. 2024). Star clusters with radii as small as ~ 1 pc were recently discovered in a highly-magnified distant galaxy at $z_{\rm spec} = 5.93$, dubbed the "Sunrise Arc" (Vanzella et al. 2023). Some of these are observed to be young massive star clusters (a few Myr old) with intense ionizing emission, while others are somewhat older (a few hundred Myr) and already gravitationally bound (Vanzella et al. 2023).

SPT0615-JD (also known as Cosmic Gems Arc), discovered by Salmon et al. (2018) in the Reionization Lensing Cluster Survey (RELICS) Hubble Treasury program (Coe et al. 2019), holds the record for being the most highly magnified and second-brightest galaxy known at $z \gtrsim 10$. Magnified to 24.5 AB mag, SPT0615-JD is several magnitudes brighter than most new $z \gtrsim 10$ candidates being discovered by JWST. Hubble Space Telescope (HST) imaging at 1.6 μm (rest-frame UV at ~ 1500 Å) identified SPT0615-JD as a $2\farcs5$-long arc (Salmon et al. 2018) and revealed small structures with radii $25 - 70$ pc (Welch et al. 2023). The superb resolution offered by NIRCam has enabled to resolve the Cosmic Gems Arc into 5 young massive star clusters (YSCs) which dominate the light of the galaxy (Adamo et al. 2024). The combination of magnified brightness and resolution make the Cosmic Gems Arc a unique lab-

oratory to conduct spatially-resolved studies with JWST not possible in any other galaxy at this distance.

In this paper, we present JWST NIRCam imaging observations of the SPT-CL J0615−5746 galaxy cluster and the Cosmic Gems Arc (SPT0615-JD), and the redshift estimate and the derived physical properties of the latter. We describe the observations in Section 2. Section 3 presents the data reduction, photometric catalogs, and photometric redshifts. Section 4 presents the lens models of the foreground galaxy cluster. Section 5 presents the results and discussion. Section 6 summarizes the results and conclusions. We use the absolute bolometric (AB) magnitude system, $m_{\mathrm{AB}} = 31.4 - 2.5\log(f_\nu \,/\mathrm{nJy})$ (Oke 1974; Oke & Gunn 1983). Where needed, we adopt a concordance cosmology with $H_0 = 70$ km s^{-1} Mpc^{-1}, $\Omega_{\mathrm{m}} = 0.3$, and $\Omega_\Lambda = 0.7$, for which $1'' \sim 4.1$ kpc at $z = 10.2$. All photometric redshift uncertainties are given at the 95% confidence level.

2. OBSERVATIONS

2.1. *JWST Data*

We obtained JWST NIRCam imaging of the galaxy cluster SPT-CL J0615−5746 (also known as PLCKG266.6−27.3) in 2023 September (JWST GO 4212; PI Bradley). The cluster has a redshift of $z_{\mathrm{spec}} = 0.972$, and has a very large mass of $M_{500} = 7.1 \times 10^{14} M_\odot h_{70}^{-1}$ (Williamson et al. 2011) for its distance.

The NIRCam observations include four short-wavelength (SW) filters (F090W, F115W, F150W, and F200W) and four long-wavelength (LW) filters (F277W, F356W, F410M, and F444W) spanning $0.8 - 5.0$ μm with 2920.4 s of exposure time in each filter. Each exposure uses the MEDIUM8 readout pattern with seven groups/integration and one integration. Four dithers were obtained with the INTRAMODULEBOX dither pattern, designed to fill the 5$''$ gaps in the NIRCam SW detectors and maximize the area with full exposure time. The dithers mitigate the effects of bad pixels, image artifacts, and flat-field uncertainties. They also improve the spatial resolution of the resampled/drizzled images. The NIRCam imaging includes two $2\rlap{.}'3 \times 2\rlap{.}'3$ fields separated by $40\rlap{.}''5$, covering 10.2 arcmin^2 in total. The SPT-CL J0615−5746 cluster was centered on NIRCam module B while NIRCam module A obtained observations on a nearby field centered $\sim 2\rlap{.}'9$ north-northwest of the cluster center. The JWST observations are shown in Figures 1 and 2 and summarized in Table 1.

2.2. *HST Data*

We supplement the JWST NIRCam observations with archival HST optical and near-infrared imaging of SPT-CL J0615−5746. Both the South Pole Telescope Survey (GO 12477; Williamson et al. 2011) and Planck collaboration (GO 12757; Planck Collaboration et al. 2011) obtained HST imaging of SPT-CL J0615−5746 with ACS/WFC F606W and F814W in 2013 January. The Reionization Lensing Cluster Survey (RELICS) HST Treasury program (GO 14096; Coe et al. 2019) obtained HST imaging of SPT-CL J0615−5746 with ACS/WFC F435W (1 orbit) and WFC3/IR F105W, F125W, F140W, and F160W (2 orbits total) in 2017. Additional HST WFC3/IR imaging was obtained in F105W (1 orbit), F125W (1 orbit), F140W (2 orbits), and F160W (2 orbits) by the RELICS team in 2020 (GO 15920; PI Salmon).

The HST observations are summarized in Table 1. In total, the JWST and HST observations of SPT-CL J0615−5746 include imaging in 15 filters spanning $0.4 - 5.0$ μm.

3. METHODS

3.1. *Data Reduction*

We reduced the pipeline-calibrated HST data and the JWST level-2 imaging products using the GRIZLI (version 1.9.5) reduction package (Brammer et al. 2022). The JWST data were processed with version 1.11.4 of the calibration pipeline with CRDS context `jwst_1123.pmap`, which includes photometric calibrations based on in-flight data.

The GRIZLI pipeline reprocesses the HST WFC3/IR data to correct exposures affected by time-variable sky backgrounds caused by scattered earthshine. For the NIRCam data, the GRIZLI pipeline applies a correction to reduce the effect of $1/f$ noise, masks "snowballs" caused by large cosmic-ray impacts, and subtracts templates to remove the "wisp" stray-light features from the NIRCam SW detectors. We aligned the HST and JWST data to a common world coordinate system registered to the GAIA DR3 catalogs (Gaia Collaboration et al. 2021). We then combined and resampled the fully-calibrated images in each filter to a common pixel grid using ASTRODRIZZLE (Koekemoer et al. 2003; Hoffmann et al. 2021). The HST and JWST NIRCam LW filter images were drizzled to a grid with 0$\rlap{.}''$04 per pixel, while the JWST NIRCam SW filter images, with their smaller native pixel scale, were drizzled to a grid with 0$\rlap{.}''$02 per pixel.

Our NIRCam SW images show the presence of stronger-than-usual wisp features that were not sufficiently removed by the wisp-template subtraction.

Table 1. HST and JWST Exposure Times and Depths

Camera	Filter	Wavelength (μm)	Exposure Time (s)	Cluster $m_{\lim}$[a] (AB)	Parallel $m_{\lim}$[a] (AB)
HST ACS/WFC	F435W	0.37–0.47	2249	27.8	28.1[b]
HST ACS/WFC	F606W	0.47–0.7	8880[c]	28.7	28.7
HST ACS/WFC	F814W	0.7–0.95	12720[d]	28.7	28.3
HST WFC3/IR	F105W	0.9–1.2	4166[e]	28.6	$\cdots$
HST WFC3/IR	F125W	1.1–1.4	3464[e]	28.6	$\cdots$
HST WFC3/IR	F140W	1.2–1.6	5874[e]	29.1	$\cdots$
HST WFC3/IR	F160W	1.4–1.7	7374[e]	28.8	$\cdots$
JWST NIRCam	F090W	0.8–1.0	2920	28.9	29.0
JWST NIRCam	F115W	1.0–1.3	2920	28.9	29.0
JWST NIRCam	F150W	1.3–1.7	2920	29.2	29.2
JWST NIRCam	F200W	1.7–2.2	2920	29.4	29.4
JWST NIRCam	F277W	2.4–3.1	2920	29.7	29.7
JWST NIRCam	F356W	3.1–4.0	2920	29.7	29.7
JWST NIRCam	F410M	3.8–4.3	2920	29.0	29.0
JWST NIRCam	F444W	3.8–5.0	2920	29.3	29.3

[a] 5σ limiting AB magnitude in a $r = 0\rlap{.}''1$ circular aperture measured on the background-subtracted data.

[b] Only a small corner of the F435W image covers the parallel field.

[c] Total exposure time includes an overlapping 2×2 mosaic centered on the cluster (GO 12477; 1920 s each) and a pointing centered on ESO 121$-$20 in the parallel field (GO 9771; 1200 s). The quoted depths represent an average over the mosaic.

[d] Total exposure time includes an overlapping 2×2 mosaic centered on the cluster (GO 12757; 2476 s each), a single pointing centered on the cluster (GO 12477; 1916 s), and a pointing centered on ESO 121$-$20 in the parallel field (GO 9771; 900 s). The quoted depths represent an average over the mosaic.

[e] Total exposure time after removing MULTIACCUM reads affected by scattered earthshine.

Wisps are caused by off-axis light from bright stars reflecting off the top secondary mirror strut of JWST and entering into the aft-optics-system mask. The wisp geometry and intensity can vary significantly depending on the exact telescope pointing. Wisps are present only in NIRCam SW images and are most prominent in the A3, A4, B3, and B4 detectors (Rigby et al. 2023).

To remove the residual wisps, we use an iterative two-dimensional (2D) background procedure using the PHOTUTILS Background2D and SourceFinder classes. We start by computing a 2D background from the drizzled image using the Background2D class with large box sizes (100×100 pixels), median-filtering over 3×3 boxes, and a sigma-clipping threshold of 3σ. We then use the SourceFinder class (with deblending turned off) to detect sources in the image larger than 50 pixels with a 2D threshold image calculated as the 2D background image plus a multiple of the background root-mean-square (rms) image. We then create a source mask from the segmentation image and dilate it using a circular footprint with a radius of 31 pixels. The dilated source mask is then input into the Background2D class with a smaller box size to compute a new background-subtracted image, from which a new source mask is created. This iterative process was repeated three times with box sizes of 100, 50, and 25 pixels, detection thresholds of 3.0, 3.0, and 1.8σ, detection pixel sizes of 50, 9, and 9 pixels, and dilation sizes of 31, 21, and 15 pixels, respectively. The final source mask was then used to compute and subtract the final background image using the Background2D class with a box size of 10×10 and median-filtered over 5×5 boxes.
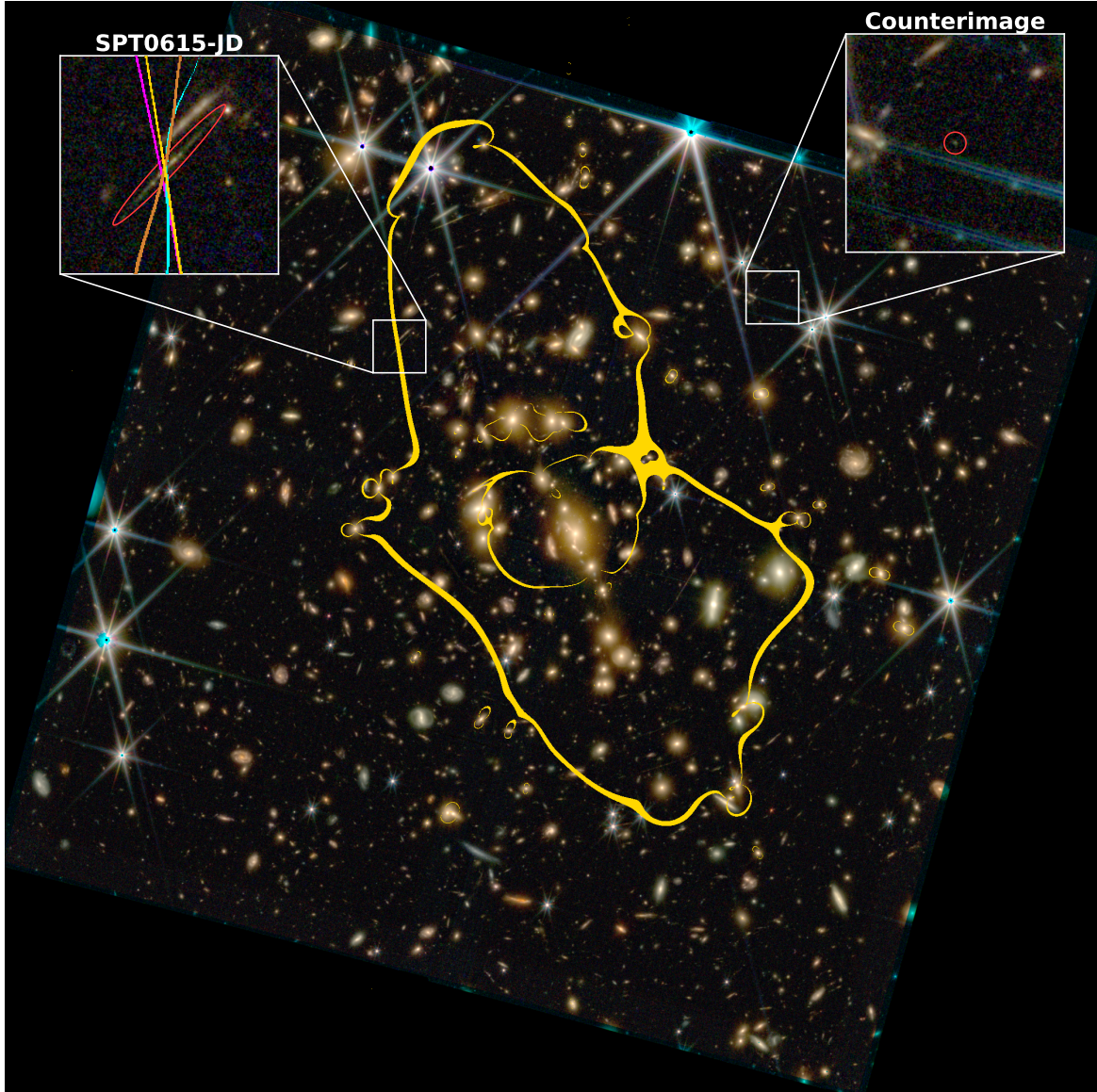
Figure 1. JWST NIRCam color image of the SPT-CL J0615−5746 cluster field (red: F115W + F150W, green: F200W + F277W, blue: F356W + F444W). The field of view is $\sim 2\rlap{.}'3 \times 2\rlap{.}'3$ and the image is shown with north up and east left. The $z = 10.2$ critical curve of our fiducial LENSTOOL-A model (see Section 4) is shown in gold. The location of the Cosmic Gems Arc is shown in the left-hand white box, with a zoomed inset figure ($8'' \times 8''$) outlining the galaxy with a red ellipse. The $z = 10.2$ critical curves of the LENSTOOL-A (gold), LENSTOOL-B (dark orange), GLAFIC (cyan), and WSLAP+ (magenta) lens models (described in Section 4) bisect the Cosmic Gems Arc. The right-hand white box and zoomed inset ($8'' \times 8''$) shows the candidate counterimage of the arc, which is located near (within $2\rlap{.}''2$) the position predicted by the lens models.

3.2. *Photometric Catalog of sources in the SPT-CL J0615−5746 region*

Sources were identified in a detection image composed of an inverse variance-weighted sum of the F277W, F356W, and F444W NIRCam LW images using PHO-TUTILS (Bradley et al. 2024) image-segmentation tools. Before performing photometry, we rebinned the NIR-Cam SW images to a pixel scale of $0\farcs04$ per pixel to put the images for all 15 filters on the same pixel-registered grid.

Photometry was measured in all bands using PHOTU-TILS SourceCatalog with the segmentation image and catalog produced from the detection image. Source colors were measured in elliptical Kron apertures with a scale factor of 1.5 to accurately recover the colors of distant galaxies. Each source has a different elliptical-aperture size and orientation based on the central moments of its flux distribution in the detection image. We derived aperture corrections by computing the ratio of the flux in a larger Kron aperture (with a Kron scale factor of 2.5) to that in the smaller aperture for each source, as measured in the detection image. We applied this aperture correction to the fluxes and uncertainties for all filters to compute total Kron fluxes. Isophotal fluxes were also calculated by summing the fluxes within the source segments defined by the segmentation image. Additional correction factors are not applied to the isophotal fluxes.

3.3. *Photometric Redshifts*

We measure photometric redshifts using EAZYPY (Brammer et al. 2008) for all sources in our catalog using the photometry measured in the elliptical Kron apertures. EAZYPY fits the observed photometry of each galaxy with a non-negative linear combination of templates to derive a probability distribution function of the redshift. We use a template set composed of the 12 "tweak_fsps_QSF_12_v3" templates derived from the Flexible Stellar Population Synthesis (FSPS) library (Conroy et al. 2009, 2010; Conroy & Gunn 2010), which include a range of galaxy types (e.g., star-forming, quiescent, dusty) and realistic star formation histories (e.g., bursts, slowly rising, slowly falling). We also include six additional templates (sets 1 and 4) from Larson et al. (2023) that are based on a combination of BPASS and CLOUDY models. These templates have bluer colors than the fiducial FSPS templates and match the predicted rest-UV colors of simulated galaxies at $z > 8$. The inclusion of these additional templates provides improvements in the photometric redshift accuracy for bluer galaxies at $z > 8$ (Larson et al. 2023).

We assume a flat luminosity prior, similar to recent JWST high-redshift studies (e.g., Finkelstein et al. 2022; Adams et al. 2023b; Finkelstein et al. 2023b), to prevent bias against selecting bright high-redshift galaxies, whose luminosity function is poorly known. We apply an error floor of 5% to the flux uncertainties to account for photometric calibration uncertainties. We allow the redshifts to span from $0.1 < z < 20$, in steps of 0.01. We also perform a second run of EAZYPY with the redshift range restricted to $z < 7$ to compare the fiducial results with the best-fit low-redshift solutions.

A recent study comparing photometric and spectroscopic redshifts for 43 $z = 7-13$ galaxies measured with EAZYPY from the JWST JADES (Rieke et al. 2023) and CEERS (Finkelstein et al. 2023b) surveys found that the photometric redshifts show exceptional agreement with the spectroscopic redshifts (Duan et al. 2024). Overall, 4.6% (2 of 43) of the sources qualify as outliers, defined as having $z_{\rm phot} > 1.15(z_{\rm spec}+1)$ or $z_{\rm phot} < 0.85(z_{\rm spec}+1)$ (Duan et al. 2024). Both of the outlier sources were at $7 < z_{\rm phot} < 8$. None of the sources at $z > 8$ were classified as outliers.

The photometric redshift catalog is available on our Cosmic Spring website.[1] The GRIZLI reduced images and catalogs are available online at the DAWN JWST Archive[2].

4. CLUSTER LENS MODELS

We generated four independent lensing models for the foreground strong-lensing galaxy cluster SPT-CL J0615−5746 to estimate source magnifications using LENSTOOL, GLAFIC, and WSLAP+. These new models are improvements over the previous SPT-CL J0615−5746 lens models presented in Paterno-Mahler et al. (2018) and Salmon et al. (2018), which were based only on HST imaging data. The different models not only span a range of modeling algorithms. Their independent construction also gives us leverage over systematic uncertainties that are due to modeling choices. The models differed in how they considered the observational constraints (e.g., whether to include candidate lensed images; photometric redshifts; including clumps within images of lensed galaxies as individual constraints; astrometric uncertainty), and choices for the parameterization of the lens plane (number of halos, substructure, and interloping masses). A more detailed comparison between the lens models will be presented in a forthcoming paper (Resseguier et al. in prep). We provide a short summary of each model below.
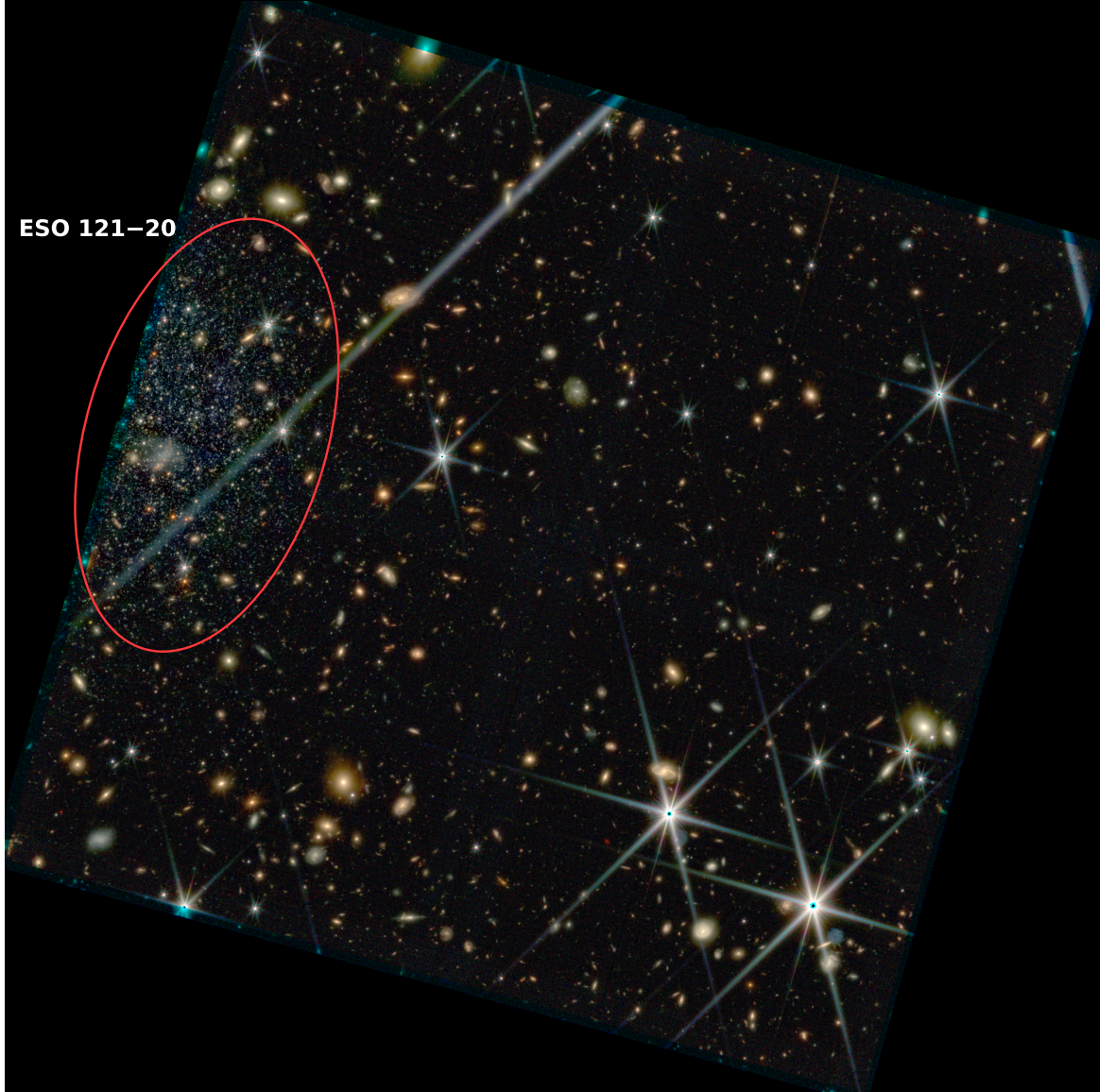
---

[1] https://cosmic-spring.github.io
[2] https://dawn-cph.github.io/dja

Figure 2. JWST NIRCam color image of the SPT-CL J0615−5746 parallel field, located north-northwest of the cluster field (red: F115W + F150W, green: F200W + F277W, blue: F356W + F444W). The field of view is $\sim 2\rlap{.}'3 \times 2\rlap{.}'3$ and the image is shown with north up and east left. The field partially includes ESO 121−20 (outlined in red), an isolated dwarf irregular galaxy at a distance of 6.05 Mpc (Karachentsev et al. 2006).

4.1. LENSTOOL *Models*

We generated two different lensing models using LENSTOOL (Jullo et al. 2007) that we refer to as LENSTOOL-A and LENSTOOL-B. LENSTOOL employs a parametric approach and MCMC sampling of the parameter space to identify the best-fit model and associated uncertainties.

For the LENSTOOL-A model, the cluster lens is represented by a combination of three main halos with contribution from cluster member galaxies, all parameterized as pseudo-isothermal ellipsoidal mass distributions (Limousin et al. 2005). Galaxy-scale halo parameters are determined using scaling relations (Jullo et al. 2007). The parameters of the two cluster-scale halos are allowed to vary, except for the cut radius that is larger than the strong lensing region and thus cannot be constrained by strong lensing evidence. The positional parameters of the brightest cluster galaxy (BCG) halo are fixed to observed values, while its slope parameters are allowed to vary. The model incorporates constraints from the positions of 43 multiple images belonging to 14 clumps from 9 distinct source galaxies. Redshifts of two spectroscopically confirmed sources at $z = 1.358$ and $z = 4.013$ (Paterno-Mahler et al. 2018) and the Cosmic Gems Arc at $z = 10.2$ are used as constraints (the A, B, and C star clusters from Adamo et al. (2024); see Figure 4). The redshifts of arcs without spectroscopic redshifts are treated as free parameters with very broad priors. While the model predicts a counterimage at (RA, Dec)=(93.9490607, −57.7701814), a potential candidate (see Figure 1) observed near this location ($\sim 1''.8$) was not used as a constraint.

External shear is not required. However, one of the cluster-scale halos is generally aligned with the galaxy distribution of the foreground group at $z = 0.42$ (Jiménez-Teja et al. 2023), possibly accounting for contributions from this structure. All observed lensed features are well-reproduced by this model. The image-plane rms of the best-fit LENSTOOL-A model is $0''.36$. The LENSTOOL-A model is used as the reference model for the analysis presented in this paper.

The LENSTOOL-B cluster lens model uses a different set of input assumptions, including a different position of the mass distribution of the lens. This model uses 43 multiple images from 11 unique sources as constraints. A secondary cluster-scale halo is placed around the location of dusty galaxies nearly $50''$ north of the BCG. The position of this halo is allowed to move within a $20''$ box around this position. The image-plane rms of the best-fit LENSTOOL-B model is $0''.68$.

4.2. GLAFIC *Model*

We construct another mass model using GLAFIC (Oguri 2010, 2021). We follow the methodology described in Kawamata et al. (2016) to determine a set of lens mass components used for mass modeling. Our mass model consists of three elliptical Navarro–Frenk–White (NFW) halos (Navarro et al. 1997), external shear, and cluster member galaxies modeled by pseudo-Jaffe ellipsoids. We fix positions of two NFW halos at the locations of bright cluster member galaxies at (RA, Dec) = (93.9663980, −57.7791580) and (93.9705078, −57.7753866), while the center of the third NFW mass halo is left as a free parameter. For all the three elliptical NFW components, we leave their masses, ellipticities, position angles, and concentration parameters as free parameters. In order to reduce the number of parameters, we adopt the standard scaling relations between the luminosities, velocity dispersions, and truncation radii of cluster member galaxies (see Kawamata et al. 2016, for more details). The observational constraints consist of the positions of 44 multiple images from 15 background sources. Spectroscopic redshifts are available for five of the 15 background sources (Paterno-Mahler et al. 2018). We fix the source redshift of Cosmic Gems Arc to $z = 10.2$. In addition, we include constraints on redshifts of six background sources based on their photometric redshifts, with a conservative error on the photometric redshifts of $\sigma_z = 0.5$ assuming the Gaussian distribution. In order to better reproduce the shape of the Cosmic Gems Arc, we also include the positions of the star cluster systems A.1/A.2 and B.1/B.2 (see Figure 4) in the Cosmic Gems Arc as constraints. We assume a positional error of $0''.4$, except for the positions of A.1/A.2 and B.1/B.2, for which we assume a smaller positional errors of $0''.04$.

The best-fitting model has $\chi^2 = 52.7$ for 37 degrees of freedom, and reproduces all multiple image positions well, with a rms of image positions of $0''.41$.

4.3. WSLAP+ *Model*

The WSLAP+ model (Diego et al. 2005, 2007) is a hybrid model combining a large-scale component for the mass and a small-scale component. The large-scale distribution of the mass is described by a predetermined grid (uniform or multi-resolution) of 2D Gaussian functions. The small-scale component follows directly the light distribution of member galaxies. The WSLAP+ lens model offers an alternative to parametric models and is free of assumptions made about the distribution of dark matter.

For the small scale, we select the most luminous elliptical member galaxies and assume their mass follows the distribution of light in the F356W filter. All galaxies

are distributed in three groups, each group with a fixed light-to-mass ratio that is optimized by WSLAP+. The first group contains the central BCG. The second group contains bright member galaxies at $z = 0.972$ ($N \approx 70$). Finally, the third group contains two foreground galaxies at $z = 0.42$ that are near other arcs in the background. This third group has negligible impact in the Cosmic Gems Arc, but it is added to the lens model to increase its precision in other portions of the image.

The smooth component is composed of either a 20×20 regular grid of 2D Gaussians or a 158 grid of 2D Gaussians. The second grid is derived from a solution obtained with the regular grid and has increased resolution in the central region of the cluster. In both cases, the amplitudes of the Gaussians are optimized by WSLAP+. We use a set of 14 multiple images as constraints from 11 individual galaxies. As in other lens models in this work, we use multiply lensed knots in several galaxies as additional constraints. The rms of the model is $\approx 1''$ (image plane) although for two systems we find a rms of $\approx 2''$, indicating a possible tension in that portion of the lens plane. These two systems are far from the $z \sim 10.2$ Cosmic Gems Arc.

5. RESULTS AND DISCUSSION

This section focuses on the analysis of the galaxy appearing as the Cosmic Gems Arc. We first present its photometric properties and discuss its photometric redshift. We describe the estimated magnifications of the arc and the detection of a candidate counterimage. Finally, we perform spectral energy distribution (SED) fitting to the multiband photometry of the Cosmic Gems Arc and discuss the intrinsic physical properties of the galaxy.

5.1. *The Cosmic Gems Arc (SPT0615-JD)*

In Figure 3, we show cutout images ($4''\!.8 \times 4''\!.8$) of the Cosmic Gems Arc in the observed HST and JWST filters. The galaxy is weakly detected in the WFC3/IR F125W image and clearly detected in F140W and all redder filters. The Cosmic Gems Arc is undetected in the JWST NIRCam F115W image and all bluer filters. While Salmon et al. (2018) reported the length of the Cosmic Gems Arc to be $2''\!.5$ from the HST WFC3/IR F160W data, the JWST data reveal faint emission that extends to $5.0''$ long in the NIRCam images.

The JWST NIRCam F150W image provides the best resolution of the Cosmic Gems Arc, revealing at least nine observed bright knots along the arc (see Figures 3 and 4). Overall, there is a distinctive symmetry of the knot locations from the center of the extended arc, suggesting that the observed arc represents two mirror im-

ages of the lensed galaxy. This is confirmed by our cluster lens models (see Section 4), all of which predict the $z = 10.2$ critical curve crossing the arc (see Figure 1 inset).

The bright knots in the Cosmic Gems Arc have been identified as individual star clusters, resolved down to 1 pc in intrinsic size in the JWST NIRCam F150W image (Adamo et al. 2024). This is the first such detection of star clusters at $z > 10$, only 460 Myr after the Big Bang, made possible by the combination of JWST's high sensitivity and spatial resolution and the gravitational lensing magnification of the Cosmic Gems Arc. The clusters have very large stellar surface densities of $\sim 10^5 \ M_\odot/pc^2$ and are consistent with gravitationally-bound YSCs (Adamo et al. 2024). These clusters could be the progenitors of metal-poor globular clusters at $z = 0$. The possibility that some progenitors of today's globular clusters have formed in low-mass galaxies at $z > 7$ is particularly interesting also because it is somewhat at odds with the predictions of several theoretical models (e.g., Reina-Campos et al. 2019), with a few exceptions (Katz & Ricotti 2013, 2014). Importantly, the high stellar densities within these systems pave the way to massive stars and stellar black hole runway collisions, which might lead to the formation of intermediate-mass black hole seeds (Gieles et al. 2018; Antonini et al. 2019).

5.2. *Photometry of the Cosmic Gems Arc*

In our initial extraction of sources in the SPT-CL J0615−5746 field, the Cosmic Gems Arc is segmented into seven separate components, labeled S1–S7, which are shown in Figure 4. We subsequently combined these segments into a single source within the segmentation image. We then measured the photometry of the Cosmic Gems Arc in all the observed HST and JWST filters using the PHOTUTILS SourceCatalog class as described in Section 3.2. As before, we measured the photometry of the Cosmic Gems Arc in both an elliptical Kron aperture with a scale factor of 1.5 and applied an aperture correction to the fluxes and uncertainties for all filters to compute total Kron fluxes. The size and shape of the elliptical Kron aperture are determined by the central moments of the flux distribution of the Cosmic Gems Arc in the detection image. This elliptical Kron aperture is shown in Figure 4. We also calculate isophotal fluxes by summing the fluxes within the combined source segments defined by the segmentation image. No
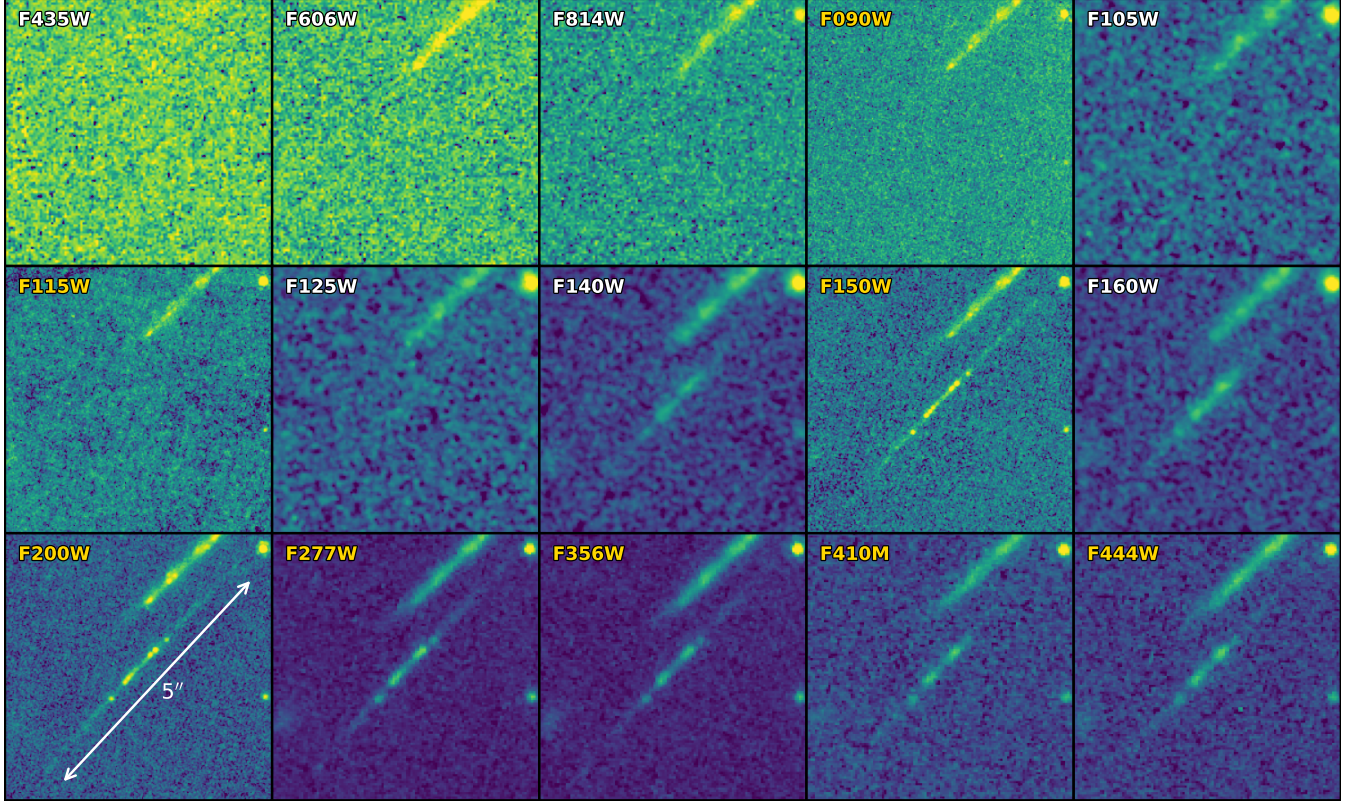
Figure 3. Cutout images of the Cosmic Gems Arc in the observed HST and JWST filters. The cutout field of view is $4\rlap{.}''8 \times 4\rlap{.}''8$ and the images are shown with north up and east left. Filters are labeled in the upper-left corner of each panel with white text for HST images and gold for JWST images. The Cosmic Gems Arc extends to $5''$ long in the JWST NIRCam images and is centered in the cutout images. The galaxy is undetected in F115W and all bluer filters. It is weakly detected in F125W and clearly detected in F140W and all redder filters. The JWST NIRCam F150W image (PSF FWHM $0\rlap{.}''05$) provides the best resolution of the Cosmic Gems Arc, revealing star clusters down to 1 pc in intrinsic size (Adamo et al. 2024). The nearby arc to the north has a photometric redshift of $z \sim 2.6$.

Table 2. Measured Photometry of SPT0615-JD with HST

ID[a]	z_{phot}[b]	F435W (nJy)	F606W (nJy)	F814W (nJy)	F105W (nJy)	F125W (nJy)	F140W (nJy)	F160W (nJy)
Kron Ellipse	$10.19^{+0.16}_{-0.16}$	5.1 ± 32.7	-17.4 ± 19.9	-8.0 ± 18.0	38.1 ± 24.1	123.8 ± 24.8	292.4 ± 16.1	543.0 ± 21.2
Sum S1–S7	$10.18^{+0.16}_{-0.16}$	12.0 ± 26.0	-0.6 ± 15.9	-3.2 ± 14.3	33.0 ± 19.2	96.1 ± 19.7	248.1 ± 12.9	447.9 ± 16.9
Sum S2–S6	$10.18^{+0.16}_{-0.16}$	7.3 ± 24.7	3.0 ± 15.0	-9.5 ± 13.6	28.3 ± 18.3	95.7 ± 18.7	236.0 ± 12.2	433.4 ± 16.1
Sum S4–S5	$10.18^{+0.16}_{-0.17}$	25.7 ± 18.7	11.0 ± 11.4	-8.9 ± 10.2	6.6 ± 13.8	61.8 ± 14.1	185.8 ± 9.3	319.0 ± 12.2
S4	$10.25^{+0.33}_{-0.23}$	14.5 ± 11.7	3.0 ± 7.1	4.0 ± 6.7	2.5 ± 8.5	25.4 ± 8.8	75.7 ± 5.7	130.7 ± 7.5
S5	$10.22^{+0.21}_{-0.19}$	11.2 ± 14.6	8.0 ± 8.9	-12.9 ± 7.7	4.1 ± 10.9	36.4 ± 11.1	110.1 ± 7.3	188.3 ± 9.6
Counterimage[c]	$10.8^{+0.6}_{-1.4}$	2.8 ± 7.2	-3.9 ± 4.2	-2.5 ± 4.7	1.5 ± 6.2	-0.6 ± 5.7	7.8 ± 3.5	9.7 ± 5.3

[a] Figure 4 shows the Kron aperture and segments S1 − S7 overplotted on the arc.

[b] Photometric redshift measured with EAZYPY. Errors are 95% confidence intervals.

[c] Photometry measured in the Kron aperture described in Section 3.2.

NOTE—Observed fluxes, uncorrected for magnification. $m_{\rm AB} = 31.4 - 2.5 \log(f_\nu/{\rm nJy})$.
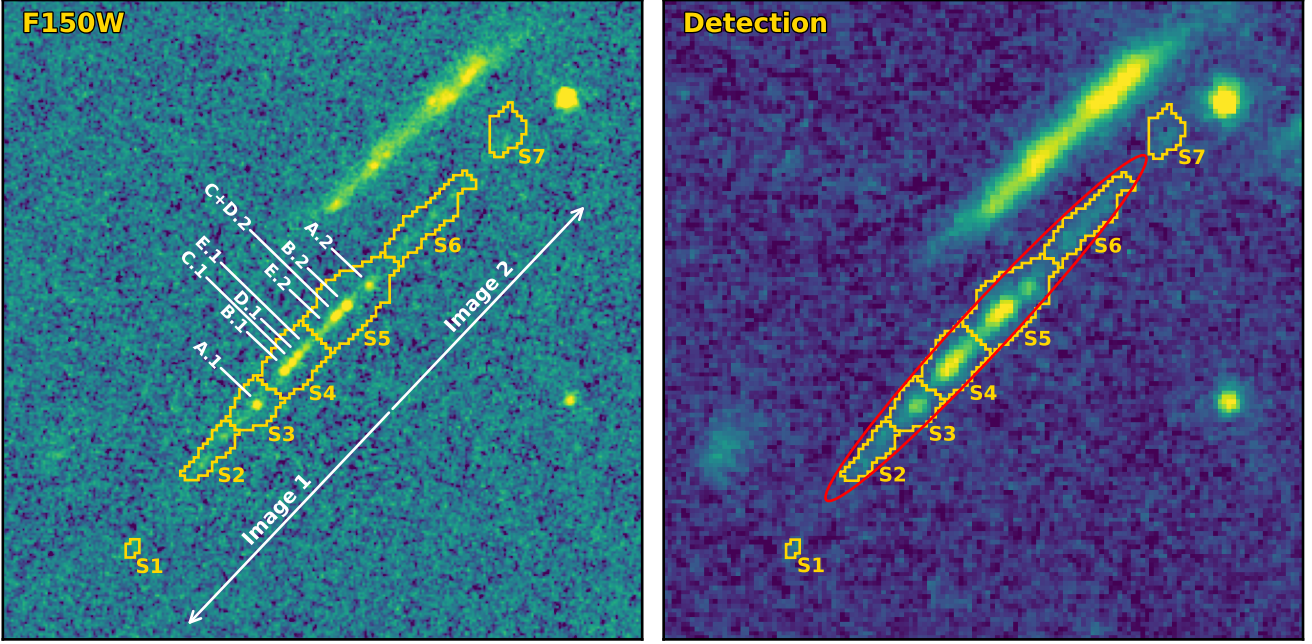
Figure 4. Cutout images ($4\rlap{.}''8 \times 4\rlap{.}''8$) of the Cosmic Gems Arc in the NIRCam F150W and detection (F277W + F356W + F444W) image. The segments S1–S7 were defined from the detection image and are outlined in gold. The Kron ellipse defined from the central moments of the flux distribution in the combined segments is shown in red. In the F150W image, we also label the two mirrored images of the arc, Images 1 and 2, as well as the star clusters A through E analyzed by Adamo et al. (2024).

Table 3. Measured Photometry of SPT0615-JD with JWST/NIRCam

ID	F090W (nJy)	F115W (nJy)	F150W (nJy)	F200W (nJy)	F277W (nJy)	F356W (nJy)	F410M (nJy)	F444W (nJy)
Kron Ellipse	1.9 ± 14.0	-4.8 ± 12.9	508.5 ± 11.6	574.0 ± 9.1	457.3 ± 8.0	368.5 ± 7.9	357.1 ± 15.3	402.2 ± 12.5
Sum S1–S7	-7.5 ± 11.1	4.2 ± 10.3	442.3 ± 9.2	491.4 ± 7.4	396.3 ± 6.5	321.6 ± 6.3	302.2 ± 12.3	350.3 ± 10.0
Sum S2–S6	-3.9 ± 10.6	6.9 ± 9.8	424.1 ± 8.8	468.9 ± 7.0	381.0 ± 6.2	306.5 ± 6.1	291.8 ± 11.8	333.4 ± 9.6
Sum S4–S5	-0.3 ± 8.0	10.6 ± 7.4	289.4 ± 6.6	337.7 ± 5.3	279.6 ± 4.9	230.4 ± 4.8	221.4 ± 9.3	254.0 ± 7.5
S4	1.8 ± 5.0	4.7 ± 4.7	119.7 ± 4.2	137.1 ± 3.4	118.8 ± 3.1	95.5 ± 3.0	95.1 ± 5.9	111.0 ± 4.8
S5	-2.1 ± 6.2	6.0 ± 5.8	169.8 ± 5.1	200.5 ± 4.2	160.9 ± 3.8	134.9 ± 3.7	126.3 ± 7.2	143.0 ± 5.8
Counterimage[b]	1.9 ± 3.1	0.2 ± 3.0	13.5 ± 2.5	15.3 ± 2.0	11.0 ± 1.5	8.4 ± 1.5	8.8 ± 3.0	6.5 ± 2.4

NOTE—Observed fluxes, uncorrected for magnification. $m_{\mathrm{AB}} = 31.4 - 2.5 \log(f_\nu/\mathrm{nJy})$.

[a] Figure 4 shows the Kron aperture and segments S1 – S7 overplotted on the arc.

[b] Photometry measured in the Kron aperture described in Section 3.2.

additional correction factors were applied, and no additional local background was subtracted.

The measured photometry of the Cosmic Gems Arc in the observed HST and JWST filters is summarized in Tables 2 and 3. We also include the photometry for a few different segment sums and the brightest two individual segments (S4 and S5) to illustrate the photometric properties of the Cosmic Gems Arc in different locations. The arc (and each of its segments) is brightest in the JWST NIRCam F200W image, with an observed magnitude of $m_{AB} = 24.5$ in the Kron aperture (including the correction to total flux) and $m_{AB} = 24.7$ in the sum of segments S1–S7. Each of the two lensed mirror images is $m_{AB} = 25.3$, similar to that observed for the brightest lensed image of MACS0647–JD at $z_{spec} = 10.17$ (Hsiao et al. 2023b) with an observed F200W magnitude of $m_{AB} = 25.1$ (Hsiao et al. 2023a). With a more modest magnification $\mu \sim 8$, MACS0647–JD is intrinsically brighter ($m_{AB} = 27.3$ delensed) than the Cosmic Gems Arc (see Section 5.4). MACS0647–JD is also observed to be slightly brighter when adding the flux from all three lensed images: $m_{AB} = 24.2$, compared to the Cosmic Gems Arc with $m_{AB} = 24.5$ (the counterimage contributing negligibly).

For comparison, the exceptionally luminous unlensed galaxy GN-z11 at $z_{spec} = 10.60$ (Bunker et al. 2023) has an observed magnitude of $m_{AB} = 26.0$ in the NIRCam F200W data (Tacchella et al. 2023). With a few exceptions of lensed galaxies, most other galaxy candidates at $z > 10$ being discovered by JWST are several magnitudes fainter (e.g., Finkelstein et al. 2023a).

5.3. *Photometric Redshifts*

The Cosmic Gems Arc has an extremely strong F115W$-$F200W break of > 3.2 mag (2σ lower limit) and is completely undetected ($< 2\sigma$) in all bluer filters. These properties, combined with a very blue continuum redward of the break, are consistent with a high-redshift Lyman-break galaxy at $z \gtrsim 10$.

We measure the photometric redshift of the Cosmic Gems Arc using EAZYPY using the same procedure described in Section 3.3. We use the photometry of the Cosmic Gems Arc in the elliptical Kron aperture, the sum of all segments (S1–S7), plus other segment sums and the brightest two individual segments (S4 and S5).

We measure the photometric redshift of the Cosmic Gems Arc to be $z_{\rm phot} = 10.19 \pm 0.16$ in the elliptical Kron aperture and $z_{\rm phot} = 10.18 \pm 0.16$ in the sum of segments S1–S7. The photometric redshifts in the various segments are all consistent with each other at $z \sim 10.2$. The photometric redshifts in the individual segments S4 and S5 are also completely consistent at

$10.25^{+0.33}_{-0.23}$ and $10.22^{+0.21}_{-0.19}$, respectively, but have larger uncertainties due to the lower signal-to-noise flux ratios in the smaller segments.

We present the best-fit SED templates and the posterior redshift distributions, P(z), in Figure 5. We also show the best-fitting SED template where we restrict the redshift to be $0.972 < z < 7$. We restrict the redshift to $z > 0.972$ as the arc is clearly lensed and thus must lie behind the galaxy cluster. The best-fit low-redshift models attempt to fit the very strong observed spectral break with a Balmer break at $z \sim 2.5$, but are unable to match the observed photometry. In all cases, the best-fit χ^2 for these "low-redshift" solutions are significantly worse than the best-fit high-redshift solutions, ruling out the low-redshift models at high significance. Formally, 97% of the P(z) probability distribution function is at $z > 10$ and increases to 100% for $z > 9.8$. The photometric redshift measurements of the Cosmic Gems Arc are summarized in Table 2.

While the photometric redshift of the Cosmic Gems Arc is highly robust, definitive confirmation of the redshift requires spectroscopic observations. In 2023 December, we also obtained JWST NIRSpec high-resolution G395H/F290LP spectroscopy (8928 s total) from the same JWST Cycle 2 program (JWST GO 4212) in several multi-shutter array slitlets along the Cosmic Gems Arc. The primary goals of these observations were to obtain a spectroscopic redshift of the galaxy and to detect and resolve the [O II] $\lambda\lambda 3726, 3729$ doublet, measuring electron densities along the arc. Incidentally, the first such detection of the resolved [O II] $\lambda\lambda 3726, 3729$ doublet at $z > 8$ was recently made from NIRSpec G395H observations of the lensed galaxy MACS0647-JD at $z = 10.17$ (Abdurro'uf et al. in prep).

Unfortunately, the spectroscopic data does not reveal any strong emission lines over the wavelength range of the observations ($2.9 - 5.3$ μm), which covers rest-frame $2636 - 4818$ Å at $z = 10.2$. The continuum was also not detected, as expected for the high-resolution G395H grating setting. Our team was recently awarded JWST cycle 3 (PI: Vanzella) observing time that includes NIRSpec prism observations of the Cosmic Gems Arc, which will be used to confirm the redshift using the Lyman-alpha break of the continuum, a technique recently used to spectroscopically confirm the redshifts of four galaxies at $10.3 \leq z \leq 13.2$ (Curtis-Lake et al. 2023).

5.4. *Magnifications*

All four of our independent lens models produce excellent results consistent with the $z = 10.2$ critical curve crossing the Cosmic Gems Arc, which confirms that the observed symmetry of the arc is indeed the result of see-
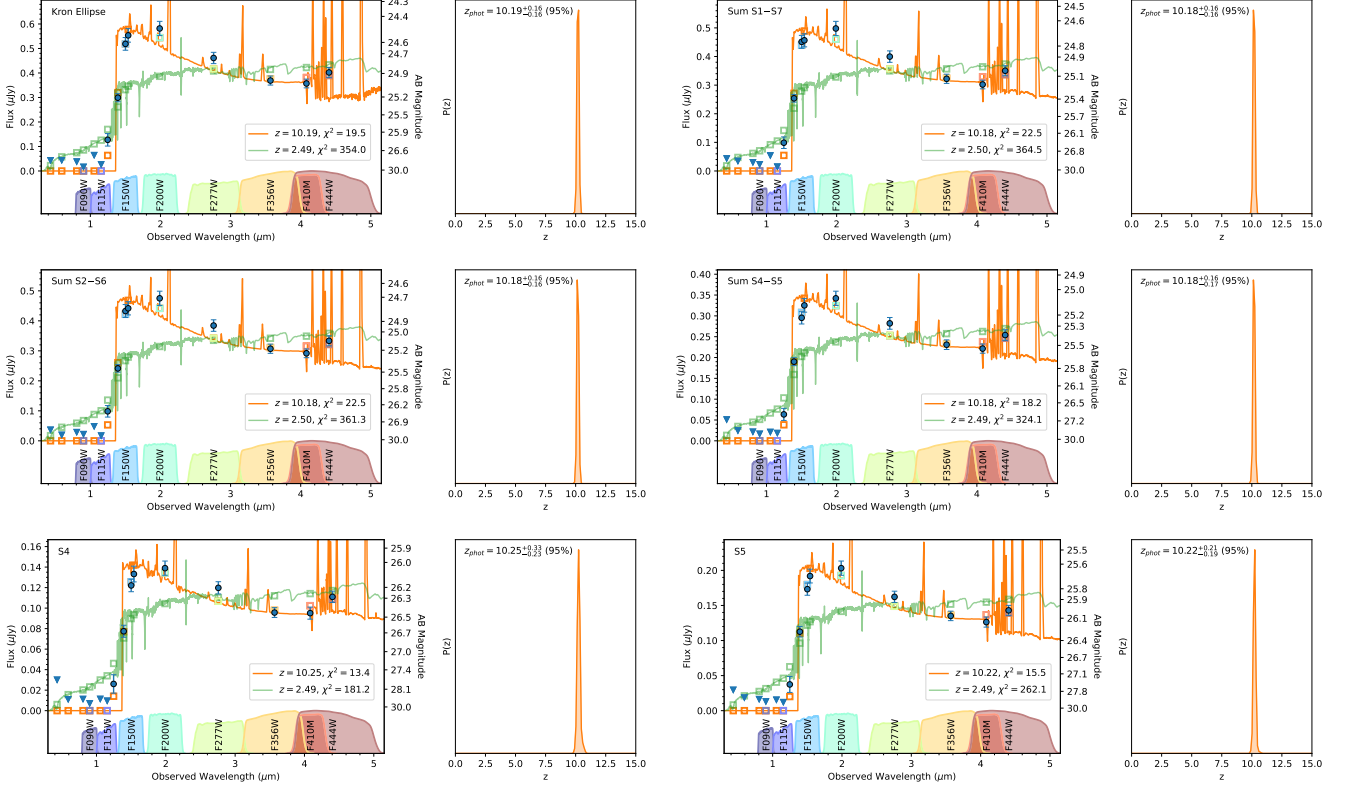
Figure 5. Best-fit EAZYPY photometric redshifts for the Cosmic Gems Arc as a whole (Kron Ellipse and Sum S1–S7) and various component segments. The measured fluxes are shown as blue data points or triangle upper limits. Nondetections are plotted as upper limits at the 2σ level. The best-fit EAZYPY SED model is shown in orange, with squares indicating the expected photometry in a given band. The best-fit EAZYPY SED for the low-redshift ($z < 7$) solution is shown in green. To the right of each SED, we also plot the P(z) posterior redshift probability distributions. The Cosmic Gems Arc has a best-fit photometric redshift of $z_{\rm phot} = 10.2$, with low-redshift solutions ruled out high significance.

ing two lensed mirror images of the galaxy (denoted in Figure 4). The $z = 10.2$ critical curve for our fiducial LENSTOOL-A model is shown in Figure 1 overlaid on the SPT-CL J0615−5746 cluster image. The Cosmic Gems Arc inset image (Figure 1) shows the critical curves from all four lens models bisecting the arc.

To verify that our results are not biased by a misinterpretation of the lensing symmetry of the arc, we ran a consistency check by excluding the positional constraints of the Cosmic Gems Arc from the lens models. For the GLAFIC and LENSTOOL-A lens models, even without this constraint, the critical curve still passes through the center of the Cosmic Gems Arc, confirming our interpretation of it being a pair of multiple images.

For the WSLAP+ lens model, when the $z = 10.2$ arc is not included as a constraint, the model predicts the critical curve passing $\sim 1''$ from the Cosmic Gems Arc. When the arc is included as a constraint, the predicted critical curve passes between the star clusters C.1 and D.1, just $0.''3$ from the alleged symmetry point in the arc and within the uncertainties typical of WSLAP+ models.

While the star clusters in the arc appear overall to be symmetric, the distance between A.1 and B.1 is greater than the distance between A.2 and B.2 by a factor of ~ 1.4. The appearance of Image 2 is likely affected by additional lensing effects from the $z_{phot} = 2.6$ arc immediately to the north of the Cosmic Gems Arc (see Figure 3). We investigated this possibility by running a WSLAP+ model that includes the $z = 2.6$ arc. While the agreement improves, it is not yet sufficient to completely explain the observed perturbation in the arc. Adding at least one other small-scale dwarf galaxy near the Cosmic Gems Arc below our current detection limit could explain the perturbed magnification of Image 2. We are exploring this possibility with a new WSLAP+ model that includes additional perturbers, but defer such analysis to future work.

Because the arc lies on the critical curve, it also has a very large magnification. The arc is highly magnified in the tangential direction along the arc, with only

modest magnification in the radial direction ($\mu \sim 1.3$). The magnifications also vary along the arc, with higher values near the critical curve, and are consistent among our lens models (see values reported in Adamo et al. (2024) at the star cluster positions). For our reference LENSTOOL-A model, the star cluster E.1 has the highest magnification of $\mu = 419$, while the star cluster A.1 has the lowest magnification of $\mu = 57$.

The light-weighted magnification of each mirrored image is $\mu \sim 60$. Assuming that we are observing two lensed images of the same galaxy, in total, the portion of the galaxy that is lensed to form the Cosmic Gems Arc is magnified by $\mu = 120$. We use this value to compute the intrinsic properties of the whole galaxy from the measured values.

The Cosmic Gems Arc has an intrinsic F200W apparent magnitude of $m_{AB} = 29.7$. This corresponds to an absolute magnitude of $M_{AB} = -17.8$ in the rest-frame UV. This makes the Cosmic Gems Arc less luminous than the typical M^* galaxy at $z \sim 10$ (e.g. Finkelstein et al. 2023a; Adams et al. 2023b), placing it in the category of galaxies likely to have driven cosmic reionization. This is especially true if the escape fraction of ionizing radiation from compact star clusters is close to unity, as suggested by some theoretical models (see, Ricotti 2002; He et al. 2020).

5.5. Candidate Counterimage

All four of our independent lens models predict a fainter counterimage of the Cosmic Gems Arc at similar locations. The reference LENSTOOL-A model predicts the counterimage at (R.A., Decl.) = (93.9490607, −57.7701814). The LENSTOOL-B predicted location is $\sim 2''$ away. The GLAFIC best model prediction is also nearby at (R.A., Decl.) = (93.9504865, −57.7696559). The WSLAP+ prediction is consistent with the other models. All the models predict a much lower magnification for the counterimage than the Cosmic Gems Arc, in the range $\mu \sim 1.5 - 2.0$.

We identify a potential candidate counterimage with the same colors of the Cosmic Gems Arc at (R.A., Decl.) = (93.95000245, −57.77021846), as shown in Figure 1. This is within $\sim 1''.8$ and $2''.2$ of the predictions from LENSTOOL-A and GLAFIC, respectively, as shown in Figure 6. The measured photometry of the candidate counterimage in the observed HST and JWST filters is summarized in Tables 2 and 3. The candidate counterimage is 3.9 mag fainter than the Cosmic Gems Arc, with an observed F200W magnitude of $m_{AB} = 28.4$, consistent with the expectation from the lens models. Earlier lens models based only on HST data (Paterno-Mahler et al. 2018; Salmon et al. 2018) predicted a coun-

terimage in proximity to our candidate, but those works were unable to identify the counterimage at the shallower depth of the HST data.

Assuming the LENSTOOL-A magnification estimate of $\mu = 2.0 \pm 0.1$ for the counterimage yields a delensed magnitude $m_{AB} = 29.2$, which is 60% brighter than the delensed magnitude estimate for the Cosmic Gems Arc of $m_{AB} = 29.7$. This may be explained by the portion of the galaxy missing in the fold of the lensing critical curve in the Cosmic Gems Arc image, whereas the counterimage is a complete image of the source galaxy. Lens model magnification uncertainties may contribute as well.

We measure a photometric redshift of $z_{phot} = 10.8^{+0.6}_{-1.4}$ for the candidate counterimage, which is consistent with the redshift of the Cosmic Gems Arc given the larger uncertainties. We present its best-fit EAZYPY SED model and the posterior redshift distribution in Figure 7.

Finally, we note according to the LENSTOOL-A model, each star cluster is magnified $\sim 3.7 - 4.7$ mag brighter in the Cosmic Gems Arc compared to the counterimage. Thus, with intrinsic magnitudes ~ 31 and fainter, none of the star clusters can be individually detected in the counterimage. Nor would they be detected without lensing in a blank field. They are only discernible thanks to the very strong lensing of the Cosmic Gems Arc.

5.6. Physical Properties

The physical properties of the Cosmic Gems Arc were estimated using the Bayesian Analysis of Galaxies for Physical Inference and Parameter EStimation (BAGPIPES) SED-fitting code (Carnall et al. 2018). BAGPIPES fits the observed photometry of a galaxy by generating model galaxy spectra over the multidimensional space of physical parameters. The fits are performed using the MULTINEST nested sampling algorithm (Feroz et al. 2009).

By default, BAGPIPES uses the stellar population synthesis models from the 2016 version of the BC03 (Bruzual & Charlot 2003) models with a Kroupa (2002) IMF. These models also include nebular line and continuum emission based on CLOUDY (Ferland et al. 2013) with the logarithm of ionization parameter (log U) allowed to vary between -4 and -2. We vary metallicity in logarithmic space from $\log Z/Z_\odot = -4$ to -0.7. Formation ages vary from 1 Myr to the age of the Universe.

We also explore the effect of using the Binary Population and Spectral Synthesis (BPASS) stellar population models (Eldridge & Stanway 2009) on the derived physi-
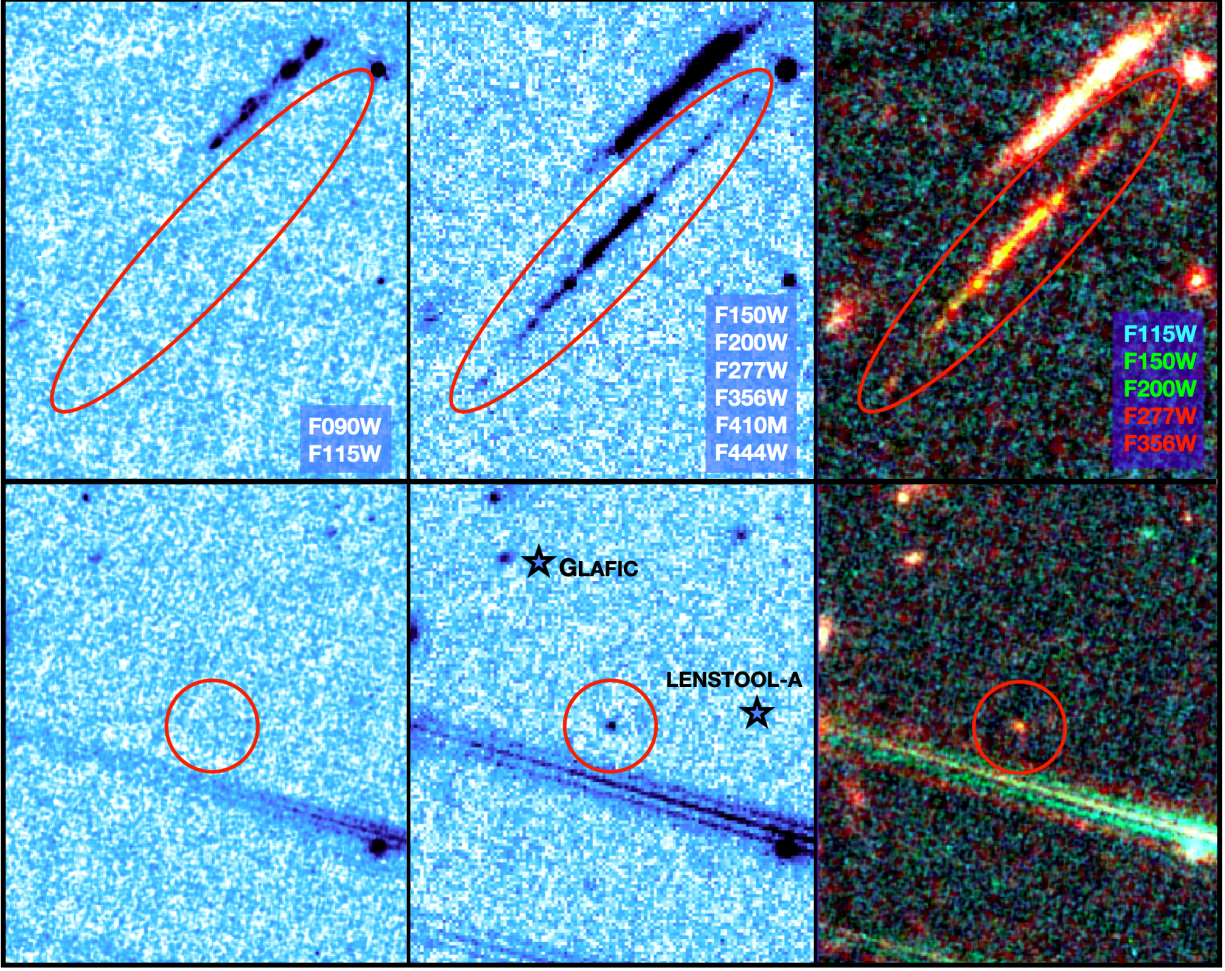
Figure 6. Cutout images of the Cosmic Gems Arc (top) and the candidate counterimage (bottom), showing the Lyman-α-break using the JWST bands only. The field of view of the cutouts is $5'' \times 6''$ and the images are shown with north up and east left. The stacked images blueward (F090W + F115W) and redward (F150W + F200W + F356W + F410M + F444W) of the Lyman-α-break are shown in the left and central panels, respectively. The right panels show color composites in the NIRCam filters. The Cosmic Gems Arc has an extremely strong NIRCam F115W−F200W break of > 3.2 mag (2σ lower limit), is undetected ($< 2\sigma$) in all bluer filters, and has a very blue continuum slope redward of the break. The candidate counterimage has similar colors to the arc, but is 3.9 mag fainter, with an observed F200W magnitude of $m_{\rm AB} = 28.4$, fully consistent with the LENSTOOL-A model prediction of the counterimage being $\sim 3.7 - 4.7$ mag fainter. The predicted locations of the counterimage from the LENSTOOL-A and Glafic models (star symbols in the bottom-center panel) are within $1''.8$ and $2''.2$ of the candidate counterimage, respectively.

cal properties. The BPASS models include binary stellar evolution and account for the effects of binary interactions on the stellar population (Eldridge et al. 2017). We use the BPASS v2.2.1 models (Stanway & Eldridge 2018) with an IMF slope of -1.30 for stars with masses $0.1-0.5\ M_\odot$, -2.35 for stars with masses $0.5-300\ M_\odot$, and a maximum stellar mass of $300\ M_\odot$.

We explore several star formation histories (SFHs) to estimate the physical properties of the Cosmic Gems Arc. The SFHs include delayed exponentially declining τ models, constant star formation rate (SFR) models, and exponentially declining models. For the delayed-τ

model, the SFR is of the form $\mathrm{SFR}(t) \propto t\ \exp{(-t/\tau)}$, where τ is the e-folding time. This SFR rises linearly with time and then exponentially declines if τ is less than the formation age.

We generally assume a Small Magellanic Cloud (SMC) dust extinction law (Salim et al. 2018). However, we also investigate the effect of using the Calzetti extinction law (Calzetti et al. 2000). For both extinction laws, we also add a second component to the dust model that includes birth-cloud dust attenuation. This attenuation is a factor of two larger around H II regions, as in the
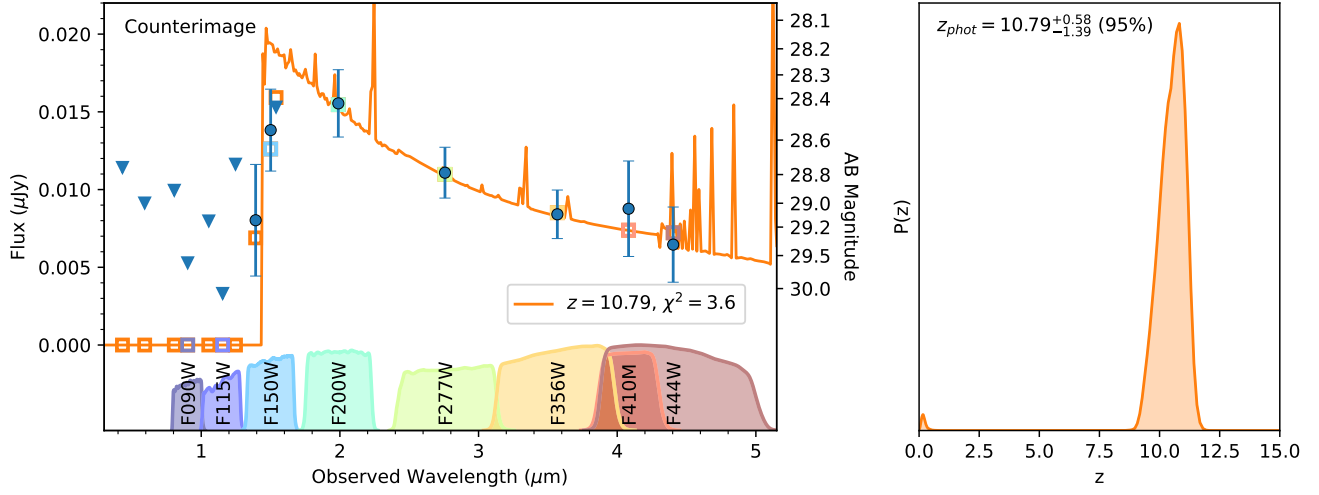
Figure 7. Best-fit EAZYPY photometric redshift for the candidate counterimage. The measured fluxes are shown as blue data points or triangle upper limits. Nondetections are plotted as upper limits at the 2σ level. The best-fit EAZYPY SED model is shown in orange, with squares indicating the expected photometry in a given band. In the right-hand panel, we plot the P(z) posterior redshift probability distribution. The candidate counterimage has a best-fit photometric redshift of $z_{\rm phot} = 10.8^{+0.6}_{-1.4}$, which is consistent with the redshift of the Cosmic Gems Arc of $z_{\rm phot} = 10.2 \pm 0.2$.
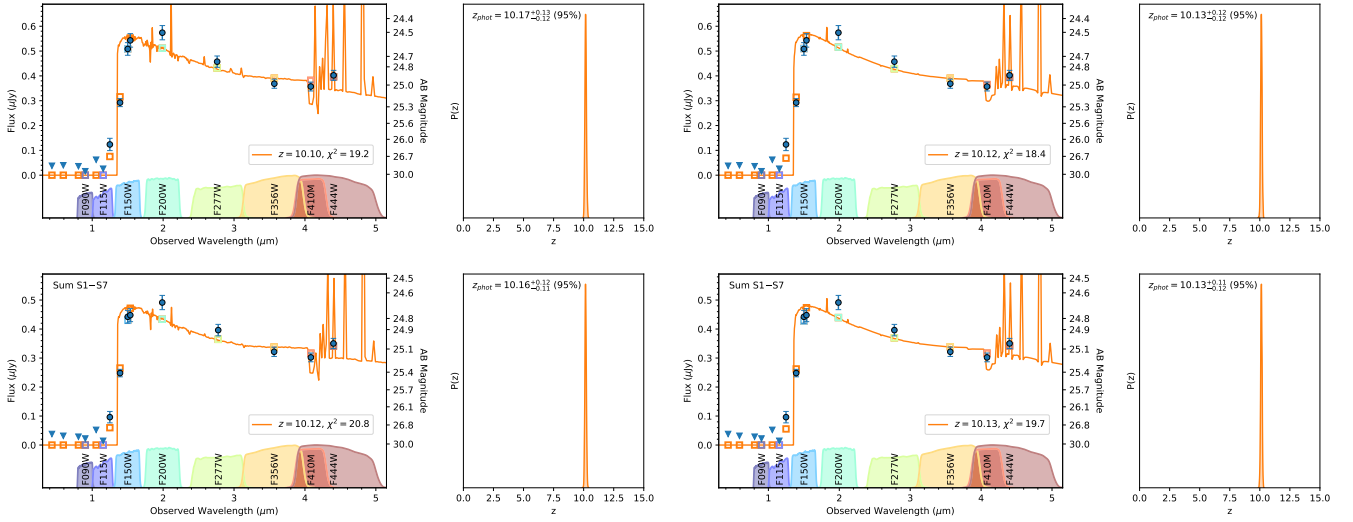
Figure 8. Best-fit BAGPIPES photometric redshifts for the Cosmic Gems Arc. The top panels show the fits to fluxes measured in the Kron Ellipse, while the bottom panels show the fits to the sum of all segments (S1–S7). The left panels show the best fits using the default BC03 stellar population models, while the right panels show the best fits using the BPASS stellar population models. The measured fluxes are shown as blue data points or triangle upper limits. Nondetections are plotted as upper limits at the 2σ level. The best-fit BAGPIPES SED model is shown in orange, with squares indicating the expected photometry in a given band. To the right of each SED, we also plot the P(z) posterior redshift probability distributions with the median $z_{\rm phot}$ and 95% confidence interval.

Table 4. BAGPIPES photometric redshifts and physical properties of SPT0615-JD

Object ID	z_{phot}[a]	$\log M_\star/M_\odot$	SFR[b] $M_\odot/yr$	$\log \mathrm{sSFR/Gyr^{-1}}$	Age[c] Myr	A_V mag	t_{form}[d] Myr
			Delayed-τ SFH model, SMC dust extinction				
Kron Ellipse	$10.2^{+0.1}_{-0.1}$	$7.47^{+0.18}_{-0.18}$	$0.33^{+0.03}_{-0.09}$	$1.05^{+0.03}_{-0.14}$	49^{+40}_{-22}	$0.02^{+0.01}_{-0.01}$	406^{+24}_{-41}
Sum S1–S7	$10.2^{+0.1}_{-0.1}$	$7.38^{+0.18}_{-0.21}$	$0.28^{+0.03}_{-0.10}$	$1.06^{+0.03}_{-0.13}$	44^{+39}_{-22}	$0.03^{+0.01}_{-0.01}$	411^{+24}_{-40}
			Delayed-τ SFH model, SMC dust extinction, BPASS stellar models				
Kron Ellipse	$10.1^{+0.1}_{-0.1}$	$7.53^{+0.12}_{-0.19}$	$0.28^{+0.01}_{-0.03}$	$0.93^{+0.13}_{-0.12}$	78^{+36}_{-36}	$0.01^{+0.01}_{-0.01}$	380^{+35}_{-36}
Sum S1–S7	$10.1^{+0.1}_{-0.1}$	$7.47^{+0.12}_{-0.17}$	$0.24^{+0.01}_{-0.02}$	$0.93^{+0.13}_{-0.12}$	79^{+38}_{-34}	$0.01^{+0.01}_{-0.01}$	378^{+34}_{-37}
			Delayed-τ SFH model, Calzetti dust extinction				
Kron Ellipse	$10.2^{+0.1}_{-0.1}$	$7.49^{+0.17}_{-0.20}$	$0.34^{+0.04}_{-0.11}$	$1.05^{+0.03}_{-0.14}$	47^{+41}_{-23}	$0.06^{+0.03}_{-0.03}$	407^{+25}_{-40}
Sum S1–S7	$10.2^{+0.1}_{-0.1}$	$7.40^{+0.20}_{-0.22}$	$0.29^{+0.05}_{-0.11}$	$1.06^{+0.02}_{-0.13}$	40^{+43}_{-21}	$0.07^{+0.03}_{-0.03}$	415^{+22}_{-45}
			Exponential SFH model, SMC dust extinction				
Kron Ellipse	$10.2^{+0.1}_{-0.1}$	$7.45^{+0.17}_{-0.13}$	$0.35^{+0.07}_{-0.10}$	$1.08^{+0.02}_{-0.08}$	36^{+30}_{-13}	$0.03^{+0.01}_{-0.01}$	419^{+14}_{-30}
Sum S1–S7	$10.2^{+0.1}_{-0.1}$	$7.39^{+0.18}_{-0.15}$	$0.30^{+0.06}_{-0.10}$	$1.08^{+0.02}_{-0.10}$	36^{+32}_{-14}	$0.03^{+0.01}_{-0.01}$	419^{+16}_{-34}
			Constant SFH model, SMC dust extinction				
Kron Ellipse	$10.1^{+0.1}_{-0.1}$	$7.75^{+0.05}_{-0.09}$	$0.68^{+0.09}_{-0.13}$	$1.08^{+0.01}_{-0.01}$	22^{+5}_{-4}	$0.14^{+0.03}_{-0.04}$	435^{+7}_{-8}
Sum S1–S7	$10.1^{+0.1}_{-0.1}$	$7.68^{+0.06}_{-0.10}$	$0.58^{+0.09}_{-0.12}$	$1.08^{+0.01}_{-0.01}$	21^{+6}_{-4}	$0.15^{+0.03}_{-0.04}$	436^{+7}_{-8}

NOTE—Properties are quoted as the median and the 68% range of the joint posterior distributions. Stellar masses and SFRs are corrected for magnification. Multiply these values by 120 / μ to apply a different magnification. We did not propagate magnification uncertainties to those parameter uncertainties.

[a] Photometric redshift with 95% confidence interval.

[b] Star formation rate during the past 100 Myr.

[c] Mass-weighted age.

[d] Formation time in Myr after the Big Bang based on the mass-weighted age.

general ISM within the galaxy's first 10 Myr. We allow dust extinction to range from $A_V = 0 - 1$ magnitudes.

We fit the observed photometry using the Kron ellipse and the sum of all segments (S1–S7) of the Cosmic Gems Arc. As with the EAZYPY fits, we apply an error floor of 5% to the flux uncertainties to account for photometric calibration uncertainties. The redshifts are allowed to span from $9.9 < z < 10.5$, based on the measured EAZYPY $z_{\rm phot} = 10.2 \pm 0.2$.

The physical properties of the Cosmic Gems Arc are presented in Table 4. The reported stellar masses and SFRs are corrected for magnification and assume that we are observing two mirror images of a galaxy, as suggested by the lens models (see Section 5.4). In Figure 8, we show the best-fit BAGPIPES SED models for the Cosmic Gems Arc, fitting both the fluxes from the Kron Ellipse and sum of segments S1–S7. Fits for both are shown for the default BC03 models and BPASS models.

For most BAGPIPES models the best-fit photometric redshift for the Cosmic Gems Arc is $z_{\rm phot} = 10.2 \pm 0.1$, in agreement with the EAZYPY photometric redshift of $z_{\rm phot} = 10.2 \pm 0.2$. Some models yield a slightly lower $z_{\rm phot} = 10.1 \pm 0.1$, but all are consistent with the EAZYPY redshift.

The intrinsic stellar masses of the Cosmic Gems Arc are consistent among the different models, with typical $\log M_\star/M_\odot$ values of $7.4 - 7.5$ ($M_* = 2.5 - 3.2 \times 10^7 \ M_\odot$). The constant SFR models yield slightly larger intrinsic stellar masses of $\log M_\star/M_\odot = 7.7 - 7.8$ ($M_* = 4.7 - 5.6 \times 10^7 \ M_\odot$). These stellar masses are lower than the typical stellar masses of $10^8 - 10^9 \ M_\odot$ found for galaxies at $z \sim 10$ (Finkelstein et al. 2022; Naidu et al. 2022; Bradley et al. 2023; Bunker et al. 2023; Hsiao et al. 2023a; Stiavelli et al. 2023).

The mass-weighted ages of the Cosmic Gems Arc indicate a relatively young stellar population, with ages typically $\sim 36 - 49$ Myr. These galaxy ages are slightly older than the ages derived for the individual star clusters, which range from 9 to 35 Myr (Adamo et al. 2024), suggesting they formed only a few tens of Myr after the galaxy and, indeed, constitute a significant fraction of the galaxy mass ($\sim 30\%$ Adamo et al. 2024). The constant SFR models yield even younger ages of $\sim 21 - 22$ Myr, while the BPASS models prefer older ages of $\sim 78 - 79$ Myr. The formation time of the Cosmic Gems Arc is $t_{\rm form} = 378 - 436$ Myr after the Big Bang.

Most models yield similar SFRs of $\sim 0.2 - 0.3 \ M_\odot/yr$ (averaged over the last 100 Myr), with the constant SFR models yielding larger SFRs of $\sim 0.6 - 0.7 \ M_\odot/yr$ with corresponding younger ages of only ~ 22 Myr. This same effect of younger ages and larger SFRs for constant

SFR models was observed for a sample of four high-redshift galaxies at $z \sim 9 - 10$ by Bradley et al. (2023).

We also find very low dust content with $A_V < 0.07$ mag for most models. For the constant SFR models, the dust extinction is slightly larger with $A_V = 0.14 - 0.15$ mag. The low dust content is consistent with the very blue rest-frame UV slope ($\beta = -2.7 \pm 0.1$) measured from a power-law fit to the F200W, F277W, and F356W photometry. These results are also consistent with the low dust extinction found in the individual star clusters from SED fitting (Adamo et al. 2024).

Finally, the best-fitting BAGPIPES results suggest a very low metallicity of $\lesssim 1\% \ Z_\odot$. While it is difficult to constrain the metallicity with the current photometric data alone, the low metallicity is consistent with the low dust content and young stellar population inferred from the SED fitting. The low metallicity is also consistent with the low metallicity ($\sim 5\% \ Z_\odot$) found in the individual star clusters of the Cosmic Gems Arc (Adamo et al. 2024). The inferred low metallicity is interesting in the context of the reionization-era galaxies, as it suggests that the Cosmic Gems Arc may be a low-metallicity or Population III (PopIII) star-forming galaxy.

The low dust content and low metallicity are also consistent with the non-detection of the dust continuum and the [O III] $88\mu m$ line from deep ALMA cycle 6 and 7 observations (PI: Tamura; program IDs 2018.1.00295.S and 2019.1.00327.S) of the Cosmic Gems Arc covering $z = 9.5 - 10.7$. The lack of any bright emission lines (including [O II] $\lambda\lambda 3726, 3729$) in the JWST NIRSpec G395H MOS observations could also be explained by low metallicity. The apparent excess of flux in the NIRCam F200W band (see Figure 8) could be due to the presence of the He II $\lambda 1640$ Å line, which is expected to be strong in low-metallicity or PopIII galaxies (e.g., Nakajima & Maiolino 2022). If the Cosmic Gems Arc is a low-metallicity or PopIII galaxy, the He II $\lambda 1640$ Å line will be clearly detected (EW > 30 Å) in the upcoming JWST Cycle 3 NIRSpec IFU prism observations of the Cosmic Gems Arc.

6. CONCLUSIONS

We present a detailed analysis of the Cosmic Gems Arc (SPT0615-JD), a galaxy candidate at $z \sim 10.2$, using a combination of recent JWST NIRCam imaging data in eight bands and archival HST imaging data in seven bands, in total spanning $0.4 - 5.0 \ \mu m$. The Cosmic Gems Arc is the most highly magnified ($\mu = 120$) and second-brightest observed galaxy known at $z \gtrsim 10$, magnified to 24.5 AB mag in the NIRCam F200W band. The combination of magnified brightness and resolution make the Cosmic Gems Arc a unique laboratory to per-

form spatially-resolved studies not possible in any other galaxy at this distance.

The Cosmic Gems Arc extends $5''$ in the JWST NIR-Cam images. There is a distinctive symmetry of bright knots from the center of the extended arc, suggesting that the observed arc represents two mirror images of the lensed galaxy. This is confirmed by our four independent cluster lens models (see Section 4), all of which predict the $z = 10.2$ critical curve crossing the arc (see Figure 1 inset). The bright knots in the Cosmic Gems Arc have been identified as five individual star clusters, resolved down to 1 pc in intrinsic size in the JWST NIR-Cam F150W image (Adamo et al. 2024). This is the first such detection of star clusters at $z > 10$, only 460 Myr after the Big Bang.

The arc has an extremely strong NIRCam F115W$-$F200W break of > 3.2 mag (2σ lower limit), is undetected ($< 2\sigma$) in all bluer filters, and has a very blue continuum slope redward of the break. Using EAZYPY, the best-fit photometric redshift for the Cosmic Gems Arc is $z_{\rm phot} = 10.2 \pm 0.2$. This is in agreement with the best-fit BAGPIPES photometric redshift of $z_{\rm phot} = 10.2 \pm 0.1$. We find that the arc is a low-luminosity galaxy ($M_{UV} = -17.8$) with a very blue rest-frame UV slope ($\beta = -2.7 \pm 0.1$). Thus, the Cosmic Gems Arc less luminous than the typical M^* galaxy at $z \sim 10$ (e.g. Finkelstein et al. 2023a; Adams et al. 2023b), placing it in the category of galaxies likely to have driven cosmic reionization.

We use the BAGPIPES code to estimate the physical properties of the Cosmic Gems Arc. Assuming a total magnification of $\mu = 120$, the intrinsic stellar mass of the Cosmic Gems Arc is $\log M_\star/M_\odot = 7.4 - 7.8$ ($M_* = 2.4 - 5.6 \times 10^7\ M_\odot$), with a mass-weighted age of $\sim 21 - 79$ Myr. The star formation rate of the Cosmic Gems Arc is $\sim 0.2 - 0.7\ M_\odot/yr$, with a very low dust content of $A_V < 0.15$ mag and a very low metallicity of $\lesssim 1\%\ Z_\odot$. The low metallicity is consistent with the low dust content and young stellar population inferred from the SED fitting, and suggests that the Cosmic Gems Arc may be a low-metallicity or PopIII star-forming galaxy.

Upcoming JWST Cycle 3 NIRSpec IFU prism observations of the Cosmic Gems Arc will provide a spectroscopic redshift and a definitive test of the low-metallicity or PopIII nature of the Cosmic Gems Arc via the He II $\lambda1640$ Å emission line. The JWST Cycle 3 observations also include MIRI MRS observations that will measure Hα emission, providing spatially-resolved maps of the star formation rates and, when combined with the NIRSpec FUV spectroscopy, the ionizing photon production efficiency, ξ_{ion}, in a young galaxy 460 Myr after the Big Bang.

7. ACKNOWLEDGMENTS

Facilities: JWST(NIRCam, NIRSpec), HST(ACS, WFC3)

Software: ASTROPY (Astropy Collaboration et al. 2022, 2018), PHOTUTILS (Bradley et al. 2024), GRIZLI (Brammer et al. 2022), EAZYPY (Brammer et al. 2008), BAGPIPES (Carnall et al. 2018),

REFERENCES

Adamo, A., Bradley, L. D., Vanzella, E., et al. 2024, arXiv e-prints, arXiv:2401.03224, doi: 10.48550/arXiv.2401.03224

Adams, N. J., Conselice, C. J., Ferreira, L., et al. 2023a, MNRAS, 518, 4755, doi: 10.1093/mnras/stac3347

Adams, N. J., Conselice, C. J., Austin, D., et al. 2023b, arXiv e-prints, arXiv:2304.13721, doi: 10.48550/arXiv.2304.13721

Antonini, F., Gieles, M., & Gualandris, A. 2019, MNRAS, 486, 5008, doi: 10.1093/mnras/stz1149

Asada, Y., Sawicki, M., Desprez, G., et al. 2023, MNRAS, 523, L40, doi: 10.1093/mnrasl/slad054

Astropy Collaboration, Price-Whelan, A. M., Sipőcz, B. M., et al. 2018, AJ, 156, 123, doi: 10.3847/1538-3881/aabc4f

Astropy Collaboration, Price-Whelan, A. M., Lim, P. L., et al. 2022, ApJ, 935, 167, doi: 10.3847/1538-4357/ac7c74

Atek, H., Shuntov, M., Furtak, L. J., et al. 2023, MNRAS, 519, 1201, doi: 10.1093/mnras/stac3144

Boyett, K., Bunker, A. J., Curtis-Lake, E., et al. 2024, arXiv e-prints, arXiv:2401.16934, doi: 10.48550/arXiv.2401.16934

Bradač, M., Strait, V., Mowla, L., et al. 2024, ApJL, 961, L21, doi: 10.3847/2041-8213/ad0e73

Bradley, L., Sipőcz, B., Robitaille, T., et al. 2024, astropy/photutils: 1.11.0, 1.11.0, Zenodo, doi: 10.5281/zenodo.10671725

Bradley, L. D., Coe, D., Brammer, G., et al. 2023, ApJ, 955, 13, doi: 10.3847/1538-4357/acecfe

Brammer, G., Strait, V., Matharu, J., & Momcheva, I. 2022, grizli, 1.5.0, Zenodo, doi: 10.5281/zenodo.6672538

Brammer, G. B., van Dokkum, P. G., & Coppi, P. 2008, ApJ, 686, 1503, doi: 10.1086/591786

Bruzual, G., & Charlot, S. 2003, MNRAS, 344, 1000, doi: 10.1046/j.1365-8711.2003.06897.x

Bunker, A. J., Saxena, A., Cameron, A. J., et al. 2023, A&A, 677, A88, doi: 10.1051/0004-6361/202346159

Calzetti, D., Armus, L., Bohlin, R. C., et al. 2000, ApJ, 533, 682, doi: 10.1086/308692

Carnall, A. C., McLure, R. J., Dunlop, J. S., & Davé, R. 2018, Monthly Notices of the Royal Astronomical Society, 480, 4379, doi: 10.1093/mnras/sty2169

Castellano, M., Fontana, A., Treu, T., et al. 2022, ApJL, 938, L15, doi: 10.3847/2041-8213/ac94d0

Castellano, M., Napolitano, L., Fontana, A., et al. 2024, arXiv e-prints, arXiv:2403.10238, doi: 10.48550/arXiv.2403.10238

Claeyssens, A., Adamo, A., Richard, J., et al. 2023, MNRAS, 520, 2180, doi: 10.1093/mnras/stac3791

Coe, D., Salmon, B., Bradač, M., et al. 2019, ApJ, 884, 85, doi: 10.3847/1538-4357/ab412b

Conroy, C., & Gunn, J. E. 2010, ApJ, 712, 833, doi: 10.1088/0004-637X/712/2/833

Conroy, C., Gunn, J. E., & White, M. 2009, ApJ, 699, 486, doi: 10.1088/0004-637X/699/1/486

Conroy, C., White, M., & Gunn, J. E. 2010, ApJ, 708, 58, doi: 10.1088/0004-637X/708/1/58

Curti, M., Maiolino, R., Curtis-Lake, E., et al. 2023, arXiv e-prints, arXiv:2304.08516, doi: 10.48550/arXiv.2304.08516

Curtis-Lake, E., Carniani, S., Cameron, A., et al. 2023, Nature Astronomy, 7, 622, doi: 10.1038/s41550-023-01918-w

Diego, J. M., Protopapas, P., Sandvik, H. B., & Tegmark, M. 2005, MNRAS, 360, 477, doi: 10.1111/j.1365-2966.2005.09021.x

Diego, J. M., Tegmark, M., Protopapas, P., & Sandvik, H. B. 2007, MNRAS, 375, 958, doi: 10.1111/j.1365-2966.2007.11380.x

Donnan, C. T., McLeod, D. J., Dunlop, J. S., et al. 2023, MNRAS, 518, 6011, doi: 10.1093/mnras/stac3472

Duan, Q., Conselice, C. J., Li, Q., et al. 2024, MNRAS, 529, 4728, doi: 10.1093/mnras/stae872

Eldridge, J. J., & Stanway, E. R. 2009, MNRAS, 400, 1019, doi: 10.1111/j.1365-2966.2009.15514.x

Eldridge, J. J., Stanway, E. R., Xiao, L., et al. 2017, PASA, 34, e058, doi: 10.1017/pasa.2017.51

Endsley, R., Stark, D. P., Whitler, L., et al. 2023, MNRAS, 524, 2312, doi: 10.1093/mnras/stad1919

Ferland, G. J., Porter, R. L., van Hoof, P. A. M., et al. 2013, RMxAA, 49, 137. https://arxiv.org/abs/1302.4485

Feroz, F., Hobson, M. P., & Bridges, M. 2009, MNRAS, 398, 1601, doi: 10.1111/j.1365-2966.2009.14548.x

Finkelstein, S. L., Bagley, M. B., Arrabal Haro, P., et al. 2022, ApJL, 940, L55, doi: 10.3847/2041-8213/ac966e

Finkelstein, S. L., Leung, G. C. K., Bagley, M. B., et al. 2023a, arXiv e-prints, arXiv:2311.04279, doi: 10.48550/arXiv.2311.04279

Finkelstein, S. L., Bagley, M. B., Ferguson, H. C., et al. 2023b, ApJL, 946, L13, doi: 10.3847/2041-8213/acade4

Gaia Collaboration, Brown, A. G. A., Vallenari, A., et al. 2021, A&A, 649, A1, doi: 10.1051/0004-6361/202039657

Gieles, M., Charbonnel, C., Krause, M. G. H., et al. 2018, MNRAS, 478, 2461, doi: 10.1093/mnras/sty1059

Hainline, K. N., Johnson, B. D., Robertson, B., et al. 2024, ApJ, 964, 71, doi: 10.3847/1538-4357/ad1ee4

Harikane, Y., Ouchi, M., Oguri, M., et al. 2023, ApJS, 265, 5, doi: 10.3847/1538-4365/acaaa9

He, C.-C., Ricotti, M., & Geen, S. 2020, MNRAS, 492, 4858, doi: 10.1093/mnras/staa165

Hoffmann, S. L., Mack, J., Avila, R., et al. 2021, in American Astronomical Society Meeting Abstracts, Vol. 53, American Astronomical Society Meeting Abstracts, 216.02

Hsiao, T. Y.-Y., Coe, D., Abdurro'uf, et al. 2023a, ApJL, 949, L34, doi: 10.3847/2041-8213/acc94b

Hsiao, T. Y.-Y., Abdurro'uf, Coe, D., et al. 2023b, arXiv e-prints, arXiv:2305.03042, doi: 10.48550/arXiv.2305.03042

Jiménez-Teja, Y., Dupke, R. A., Lopes, P. A. A., & Vílchez, J. M. 2023, A&A, 676, A39, doi: 10.1051/0004-6361/202346580

Jullo, E., Kneib, J. P., Limousin, M., et al. 2007, New Journal of Physics, 9, 447, doi: 10.1088/1367-2630/9/12/447

Karachentsev, I. D., Dolphin, A., Tully, R. B., et al. 2006, AJ, 131, 1361, doi: 10.1086/500013

Katz, H., & Ricotti, M. 2013, MNRAS, 432, 3250, doi: 10.1093/mnras/stt676

—. 2014, MNRAS, 444, 2377, doi: 10.1093/mnras/stu1489

Kawamata, R., Oguri, M., Ishigaki, M., Shimasaku, K., & Ouchi, M. 2016, ApJ, 819, 114, doi: 10.3847/0004-637X/819/2/114

Koekemoer, A. M., Fruchter, A. S., Hook, R. N., & Hack, W. 2003, in HST Calibration Workshop : Hubble after the Installation of the ACS and the NICMOS Cooling System, 337

Kroupa, P. 2002, Science, 295, 82, doi: 10.1126/science.1067524

Larson, R. L., Hutchison, T. A., Bagley, M., et al. 2023, ApJ, 958, 141, doi: 10.3847/1538-4357/acfed4

Limousin, M., Kneib, J.-P., & Natarajan, P. 2005, MNRAS, 356, 309, doi: 10.1111/j.1365-2966.2004.08449.x

Matthee, J., Mackenzie, R., Simcoe, R. A., et al. 2023, ApJ, 950, 67, doi: 10.3847/1538-4357/acc846

McLeod, D. J., Donnan, C. T., McLure, R. J., et al. 2023, MNRAS, doi: 10.1093/mnras/stad3471

Mowla, L., Iyer, K. G., Desprez, G., et al. 2022, ApJL, 937, L35, doi: 10.3847/2041-8213/ac90ca

Mowla, L., Iyer, K., Asada, Y., et al. 2024, arXiv e-prints, arXiv:2402.08696, doi: 10.48550/arXiv.2402.08696

Naidu, R. P., Oesch, P. A., van Dokkum, P., et al. 2022, ApJL, 940, L14, doi: 10.3847/2041-8213/ac9b22

Nakajima, K., & Maiolino, R. 2022, MNRAS, 513, 5134, doi: 10.1093/mnras/stac1242

Navarro, J. F., Frenk, C. S., & White, S. D. M. 1997, ApJ, 490, 493, doi: 10.1086/304888

Oguri, M. 2010, PASJ, 62, 1017, doi: 10.1093/pasj/62.4.1017

—. 2021, PASP, 133, 074504, doi: 10.1088/1538-3873/ac12db

Oke, J. B. 1974, ApJS, 27, 21, doi: 10.1086/190287

Oke, J. B., & Gunn, J. E. 1983, ApJ, 266, 713, doi: 10.1086/160817

Paterno-Mahler, R., Sharon, K., Coe, D., et al. 2018, ApJ, 863, 154, doi: 10.3847/1538-4357/aad239

Planck Collaboration, Aghanim, N., Arnaud, M., et al. 2011, A&A, 536, A26, doi: 10.1051/0004-6361/201117430

Reina-Campos, M., Kruijssen, J. M. D., Pfeffer, J. L., Bastian, N., & Crain, R. A. 2019, MNRAS, 486, 5838, doi: 10.1093/mnras/stz1236

Ricotti, M. 2002, MNRAS, 336, L33, doi: 10.1046/j.1365-8711.2002.05990.x

Rieke, M. J., Robertson, B., Tacchella, S., et al. 2023, ApJS, 269, 16, doi: 10.3847/1538-4365/acf44d

Rigby, J., Perrin, M., McElwain, M., et al. 2023, PASP, 135, 048001, doi: 10.1088/1538-3873/acb293

Roberts-Borsani, G., Treu, T., Chen, W., et al. 2023, Nature, 618, 480, doi: 10.1038/s41586-023-05994-w

Robertson, B., Johnson, B. D., Tacchella, S., et al. 2023, arXiv e-prints, arXiv:2312.10033, doi: 10.48550/arXiv.2312.10033

Salim, S., Boquien, M., & Lee, J. C. 2018, ApJ, 859, 11, doi: 10.3847/1538-4357/aabf3c

Salmon, B., Coe, D., Bradley, L., et al. 2018, ApJL, 864, L22, doi: 10.3847/2041-8213/aadc10

Stanway, E. R., & Eldridge, J. J. 2018, MNRAS, 479, 75, doi: 10.1093/mnras/sty1353

Stiavelli, M., Morishita, T., Chiaberge, M., et al. 2023, ApJL, 957, L18, doi: 10.3847/2041-8213/ad0159

Tacchella, S., Eisenstein, D. J., Hainline, K., et al. 2023, ApJ, 952, 74, doi: 10.3847/1538-4357/acdbc6

Vanzella, E., Castellano, M., Bergamini, P., et al. 2022, ApJL, 940, L53, doi: 10.3847/2041-8213/ac8c2d

Vanzella, E., Claeyssens, A., Welch, B., et al. 2023, ApJ, 945, 53, doi: 10.3847/1538-4357/acb59a

Welch, B., Coe, D., Zitrin, A., et al. 2023, ApJ, 943, 2,
doi: 10.3847/1538-4357/aca8a8

Williamson, R., Benson, B. A., High, F. W., et al. 2011,
ApJ, 738, 139, doi: 10.1088/0004-637X/738/2/139